Research Article

Tong Jiao, Chuhong Pu, Qiang Xu*, Minggao Tang*, Xing Zhu*, Chuankun Liu, and Jiang Li

Development and characterization of a coaxial strain-sensing cable integrated steel strand for wide-range stress monitoring

https://doi.org/10.1515/rams-2023-0165 received October 16, 2023; accepted December 23, 2023

Abstract: Monitoring the stress of steel strands, from initial tension to eventual failure, is paramount for assessing structural safety and understanding its failure mechanism. Current monitoring methods are restricted in measuring stress only until yielding because of their limited range. This study proposes a novel coaxial strain-sensing cable (CSSC) based intelligent steel strand (CSSC-ISS), which has both functions of force-bearing and self-sensing. First, the prototype design of CSSC-ISS and the sensing principle of CSSC are introduced. Then, a fabrication method of small-diameter CSSC is proposed, which is then encapsulated with glass fiber reinforced polymer (GFRP) material, forming a GFRP sensing rod (GFRP-SR). The next step involves replacing the strand's central wire with the GFRP-SR, culminating in the creation of the CSSC-ISS. Finally, Laboratory tests

show that the CSSC has excellent strain-sensing performance with a resolution of at least 100 $\mu\epsilon$ and a measurement range of 150,000 $\mu\epsilon$. The GFRP-SR offers good sensing potential and comparable mechanical strength to standard GFRP rods. Notably, the CSSC-ISS could measure stress up to strand failure, retaining 87.9% tensile strength and 88.7% elastic modulus compared to standard steel strands. It is verified that the CSSC-ISS can consistently measure its stress condition throughout its life cycle without compromising its load-bearing potential.

Keywords: steel strand, wide-range stress sensing, coaxial strain-sensing cable

1 Introduction

Steel strand is a high-strength load-bearing component widely used in many civil engineering structures, including precast-reinforced concrete structures, bridge cables, foundation engineering, tunnels, long-span structures, and coalmine engineering [1]. The stress state of these strands directly impacts structural safety. Consequently, monitoring the stress of steel strands, from initial tension to failure, is pivotal for structural safety evaluation and failure mechanism analysis [2,3]. Therefore, it is particularly important to develop a monitoring technique that can measure steel strand stress throughout its entire life cycle.

Various techniques, including guided ultrasonic waves [4–6], electromagnetic (EM) oscillation method [7], electrical resistance [8], piezoceramic transducer [9], magnetoelastic inductance method [10], and magnetic flux method [11,12], have been explored for measuring steel strand stress. Although these methods can accurately measure the stress of the steel strands, they are unsuitable for long-term online monitoring in practical projects due to challenges like poor moisture resistance, durability, measurement stability, and installation difficulties in harsh environments. For example, Le *et al.* developed a low-cost piezoelectric (PZT)-based intelligent strand prepared by embedding a cheap and high-sensitive electromechanical

Chuankun Liu: College of Environment and Civil Engineering, Chengdu University of Technology, Chengdu, 610059, China; Sichuan Academy of Environmental Policy and Planning, Chengdu, 610041, China

Jiang Li: Sichuan Institute of Geological Engineering Investigation Group Co., Ltd, Chengdu, 610072, China

^{*} Corresponding author: Qiang Xu, State Key Laboratory of Geohazard Prevention and Geoenvironment Protection (Chengdu University of Technology), Chengdu, 610059, China; College of Environment and Civil Engineering, Chengdu University of Technology, Chengdu, 610059, China, e-mail: xq@dlut.edu.cn

^{*} Corresponding author: Minggao Tang, State Key Laboratory of Geohazard Prevention and Geoenvironment Protection (Chengdu University of Technology), Chengdu, 610059, China; College of Environment and Civil Engineering, Chengdu University of Technology, Chengdu, 610059, China, e-mail: tomyr2008@163.com

^{*} Corresponding author: Xing Zhu, State Key Laboratory of Geohazard Prevention and Geoenvironment Protection (Chengdu University of Technology), Chengdu, 610059, China, e-mail: zhuxing15@cdut.edu.cn Tong Jiao: State Key Laboratory of Geohazard Prevention and Geoenvironment Protection (Chengdu University of Technology), Chengdu, 610059, China; College of Environment and Civil Engineering, Chengdu University of Technology, Chengdu, 610059, China Chuhong Pu: College of Environment and Civil Engineering, Chengdu University of Technology, Chengdu, 610059, China

impedance (EMI) sensor into a seven-wire steel strand. The intelligent strand can accurately predict the prestress force of steel strands using the EMI response [13,14]. It provides a promising technology for prestress monitoring. However, the intelligent steel strand (ISS) involves bonding the PZT patch onto a thin beam-like structure, which is then secured to the outer surface of the steel strand. The quality of contact between PZT and the beam-like structure will influence the sensing performance of the steel strand. This can render it challenging to install in specific confined spatial scenarios, such as those encountered in the application of adhesive prestressed steel strands. Simultaneously, limitations are evident in terms of installation challenges, particularly in confined spatial scenarios, such as those encountered in the application of adhesive prestressed steel strands. As optical fiber sensors are widely used in structural health monitoring [15,16], many scholars also study their application in stress monitoring of steel strands. The common approach involves attaching the optical fiber sensor directly to the steel strands [17-21]. A more innovative approach is to integrate optical fiber and steel strands into an integrated structure, termed "ISS." For example, Zhou et al. developed an fiber Bragg gratings (FBG)-based smart steel strand where the strand's central wire was replaced with a glass fiber reinforced polymer (GFRP)-FBG rod, enabling realtime local stress sensing by using the built-in FBG without compromising its load-bearing capacity [22,23]. This concept evolved into another version using distributed optical fiber in place of FBG [24,25]. Besides, Kim et al. conducted a comprehensive investigation of optical fiber-based ISSs. They developed a strand by inserting an optical fiber sensor inside a tube installed in the central wire of the strand. This innovative approach was then applied to measure the prestressing force and strain of seven-wire steel strands, which are widely used for prestressed concrete members [26–28]. Though these optical fiber-based intelligent strands present a promising solution, their limited measuring range

restricts their capability to monitor post-yield stress evolution in steel strands. For example, Kim et al. inserted common FBG coated with acrylate into a seven-wire steel strand and obtained a maximum strain measurement of 6517.16 µE, as shown in Figure 1 [29]. While in practical applications, the pretension strain of prestressed steel strand is as high as 6,000–7,000 με, its yield strain is often more than 9,000 µE, and the ultimate strain is usually more than 13,000 µE or even higher. Previous research indicates that these optical fiber-based strands cover merely 75% of a strand's ultimate strain [30]. To address this limitation, Kim et al. conducted some work to enhance the measurement range of optical fiber-based ISSs. They developed an ISS capable of measuring strain up to a range of 13,000–14,000 με by replacing the steel core wire with a carbon core wire, where the acrylate-coated FBG is embedded in the carbon core wire [31]. Another approach to enhance the strain measurement range of ISSs involves the utilization of polyimide-coated FBGs as sensing elements. Experimental validation has demonstrated that this type of FBG possesses a range of approximately 55,000 με [32,33]. Kim et al. inserted this polyimide-coated FBG into a polyimide protective tube and then embedded them into the steel strand, achieving a maximum strain measurement of up to 23,600 με [32]. Although optical fiber-based ISSs have made significant progress, optical fiber is small and fragile and can easily break when subjected to a shear force [34,35]. Therefore, probably the primary practical concern with optical fiberbased ISSs is to ensure that the optical fiber, especially the leading optical cable, is not damaged during the installation or measurement process or in a harsh construction environment. There is still a need to develop a stress monitoring method for steel strands that is both highly robust and offers a large measurement range.

Inspired by the structural similarities and shared EM wave transmission mechanisms between coaxial cables and optical fibers, the elongation of coaxial cables is

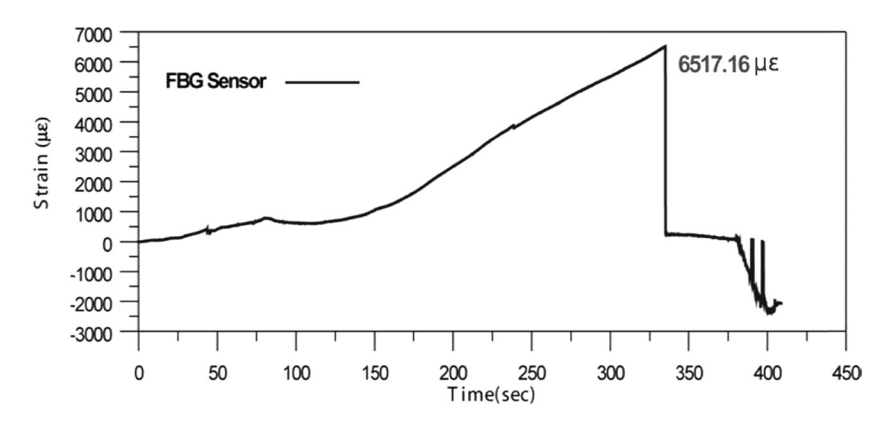


Figure 1: Strain measurements of FBG embedded in steel strand conducted by Kim et al. [29].

much higher than that of optical fibers. Researchers have adapted optical fiber sensing mechanisms such as fiber Bragg gratings, long-period gratings, and Fabry-Perot interferometry onto coaxial cables, resulting in the development of coaxial cable Bragg gratings (CCBG) [36–38], long-period Bragg gratings [39], and coaxial cable Fabry-Perot interferometer [40-42]. Each of these coaxial cable-based sensors has a large strain measurement capability of at least 150,000 με, making them an ideal candidate for stress monitoring of strands from initial tension to ultimate damage. Nevertheless, these coaxial cable-based sensors remain in the stages of laboratory principle research and performance verification and have not yet realized practical engineering applications. Further exploration is required to harness these sensors for steel strand stress monitoring. This encompasses the development of fabrication and encapsulation processes for small-diameter coaxial cable sensors to ensure seamless integration into strands without significant perturbation to the strand stress field. Further, the mechanical coupling properties of the sensor and the strands, as well as the sensing properties of the sensor, also need to be investigated experimentally.

In this study, a small-diameter coaxial strain-sensing cable (CSSC) was developed based on the CCBG sensing mechanism. Following the same idea of optical-fiber-based ISSs, we developed a CSSC-based ISS (CSSC-ISS) capable of large-strain measurements. First, we introduced the design of the CSSC-ISS prototype and the sensing mechanism of CSSC. Then, employing the SF047 coaxial cable, we proposed a fabrication method for the small-diameter CSSC and evaluated its sensing performance. Subsequently, we used glass fiber reinforced polymer (GFRP) to package the CSSC, creating a GFRP sensing rod (GFRP-SR). This GFRP-SR then replaced the central wire in a standard steel strand, resulting in the development of the CSSC-ISS. Finally, the sensing properties of CSSC and the mechanical and sensing properties of GFRP-SR and CSSC-ISS were tested through a series of laboratory tests.

2 Materials and methods

2.1 Prototype design of CSSC-ISS

In this study, a 1×7 standard prestressed steel strand of 1,860 MPa strength and 15.2 mm nominal diameter is used to develop CSSC-ISS. As shown in Figure 2, the CSSC-ISS consists of the CSSC, a GFRP protective layer, high ductility copper foil, and a steel-stranded outer wire from the inside to the outside. Here the CSSC acts as a large strain sensing unit. The CSSC is built into the GFRP layer, forming a GFRP-SR that has both load-bearing and sensing functions. Multiple layers of ductile copper foils are helically wrapped around the GFRP-SR, augmenting the bond stress between the GFRP-SR and the steel strand's outer wires. In practical engineering applications, anchors are used to install CSSC-ISS in the structures. When prestress is applied, the steel strand's outer wires twist, boosting the bond between the GFRP-SR and the strand's outer wires, thus making them deform cooperatively. The strain measured by the CSSC within the GFRP-SR corresponds to the strand's strain. Utilizing Hooke's law, the stress of the CSSC-ISS can be obtained from Eq. (1).

$$\sigma = E_{\text{CSSC-ISS}}\varepsilon,\tag{1}$$

where σ is the stress of the CSSC-ISS; $E_{\text{CSSC-ISS}}$ is the elastic modulus of the CSSC-ISS; and ε is the strain measurements of the CSSC.

2.2 CSSC and its working principle

A coaxial cable is a microwave transmission line, which includes a cylindrical inner conductor, a tubular insulation material, and a hollow outer conductor from the inside to the outside, and the three are coaxially arranged. A CSSC is developed on a coaxial cable. As depicted in Figure 3, a typical CSSC is characterized by multiple weak, periodic impedance discontinuities along its length. According to the transmission line theory, each of these discontinuities results in a slight reflection of the propagating EM wave inside the cable. When these discontinuities are uniform, their cumulative reflections can phase-align, producing a reflectance spectrum with pronounced peaks at certain frequencies (known as resonant frequencies) and a transmission spectrum with a band gap, as shown in Figure 4.

According to Huang [43], the discrete resonant frequencies in the reflectance spectrum or transmission spectrum satisfy the following Bragg condition:

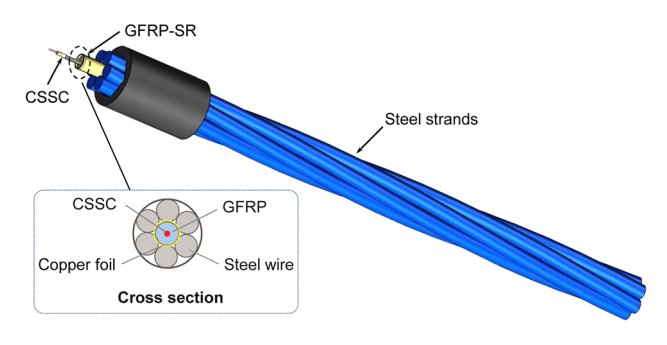


Figure 2: Schematic of the CSSC-ISS.

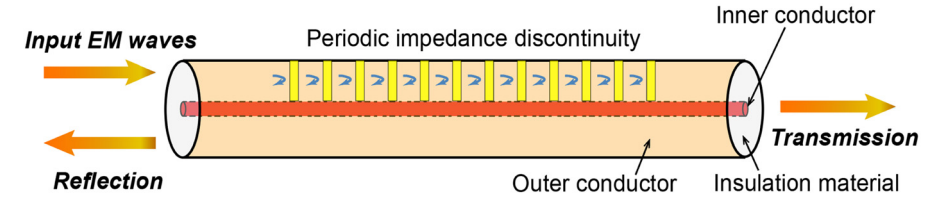


Figure 3: Schematic drawing of CSSC.

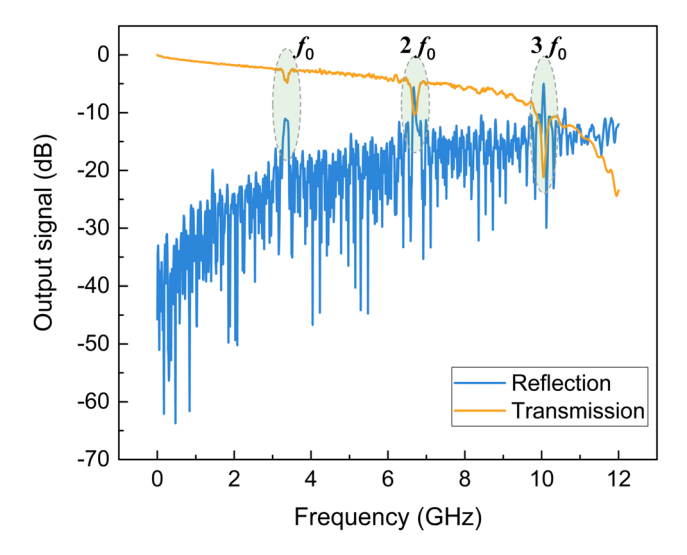


Figure 4: Reflectance and transmission spectra of CSSC.

$$f_{\rm res}^N = \frac{Nc}{2\Lambda\sqrt{\epsilon_{\rm r}}}.$$
 (2)

Taking a derivative, the formula can be expressed as:

$$\frac{\Delta f_{\text{res}}^{N}}{f_{\text{res}}^{N}} = -\frac{\Delta \Lambda}{\Lambda} - \frac{\Delta \sqrt{\epsilon_{\text{r}}}}{\sqrt{\epsilon_{\text{r}}}},\tag{3}$$

where $\in_{\mathbf{r}}$ is the dielectric constant of insulation material; Λ is the spacing of adjacent discontinuities; c is the velocity of EM wave in vacuum; f_{res}^N represents the Nth resonant frequency, and Δf_{res}^N represents the Nth resonant frequency shift.

The applied axial strain will cause an elongation of the CSSC and decrease the dielectric constant due to the photoelastic effect. These are the dominant factors inducing the resonant frequency shift. Therefore, the strain (ε) can be expressed in terms of changes in the spacing of discontinuities $(\Delta\Lambda)$ and relative permittivity $(\Delta\sqrt{\epsilon_r})$ as follows:

$$\varepsilon = \frac{\Delta \Lambda}{\Lambda} \text{ and } \frac{\Delta \sqrt{\epsilon_{\rm r}}}{\sqrt{\epsilon_{\rm r}}} = -\frac{\epsilon_{\rm r}}{2} [p_{12} - \nu(p_{11} + p_{12})] \varepsilon$$

$$= -p_{\rm off} \varepsilon. \tag{4}$$

where p_{11} and p_{12} are the Pockels coefficients of the inner dielectric, ν is the Poisson ratio of the dielectric, and $P_{\rm eff}$ is the effective coefficient.

For coaxial cable with polyethylene dielectric material, the reference values of p_{11} , p_{12} , and ν are 0.337, 0.327, and 0.27, respectively. So, the $\Delta f_{\rm res}^N$ can be derived from Eqs. (3) and (4) as follows:

$$\frac{\Delta f_{\text{res}}^{N}}{f_{\text{res}}^{N}} = -0.778\varepsilon. \tag{5}$$

Eq. (5) proves that the resonant frequency shift and strain are linear, which is the theoretical basis of strain sensing of CSSC. In practical applications, a vector network analyzer (VNA) can be used to capture the resonant frequency change of the CSSC spectrum, and the strain can be calculated using Eq. (5).

2.3 Fabrication of the CSSC-ISS

The fabrication of CSSC-ISS involves three steps: (1) preparing a small-diameter CSSC; (2) packaging the CSSC with GFRP to produce GFRP-SR; (3) assembling the GFRP-SR and steel wires to form the CSSC-ISS. The detailed procedures for each step are described in Sections 2.3.1–2.3.3.

2.3.1 Preparation of small-diameter CSSC

Coaxial cables come in various diameters, ranging from less than 1 mm to over 11.5 mm. To ensure that the diameter of the GFRP-SR matches the 5 mm diameter of a steel strand's central wire while maintaining sufficient mechanical strength, it is crucial that the CSSC's diameter is neither too large to weaken the GFRP-SR nor too small to complicate the creation of impedance discontinuities. For this purpose, an SF047 coaxial cable with a diameter of 1.19 mm is chosen.

The key of CSSC fabrication is to create impedance discontinuities on the coaxial cable. The theoretical expression of the coaxial cable's characteristic impedance is:

$$Z_0 = \frac{60}{\sqrt{\epsilon_r}} \ln \left(\frac{D_0}{D_i} \right), \tag{6}$$

where D_0 and D_i represent the outer and inner diameters of the tubular insulation layer, respectively.

According to Eq. (6), impedance discontinuity can be achieved by changing the dielectric constant of the insulation material or altering the ratio of the insulation layer's inner to outer diameters. While the drilling-hole method for creating impedance discontinuities is discussed by Huang [43], it is not applicable for small-diameter CSSCs due to the challenges of drilling such thin cables. In this study, impedance discontinuities are introduced by crimping thin-walled metal ferrules onto the cable. This approach modifies the ratio of D_0 and D_i in Eq. (6).

The fabrication procedures of impedance discontinuities are as follows: (a) Sliding several 10 mm long thinwalled metal ferrules onto the coaxial cable, positioning each ferrule according to the designated discontinuity location; (b) Soldering RF connectors at the cable's ends and connecting them to the VNA's ports 1 and 2; (c) Using a hydraulic clamp comprising two extruded blocks with round holes (Figure 5) to compress the metal ferrules. This compression achieves precise deformation, resulting in stable impedance discontinuities. For a high-quality CSSC, the reflection coefficients of each impedance discontinuity should be roughly equal. During the ferrule crimping process, realtime observation of these coefficients using the VNA is essential. Adjustments to the crimp depth of the metal ferrules can modify the reflection coefficients. The objective is to adjust all coefficients to approximate 1%.

The number of impedance discontinuities impacts the sensing signal quality. As depicted in Figure 6, with an increase in the number of discontinuities (*N*), the resonance peak at the fundamental frequency also rises. Notably, when

there are 40 reflection points, the signal-to-noise ratio (SNR) of the resonant peak in the transmission spectrum exceeds 8 dB. This indicates that for demodulation requirements, there should be over 40 discontinuities. Therefore, the CSSC was designed with 41 discontinuities spaced at 20 mm intervals for this study, as shown in Figure 7.

2.3.2 Packaging of CSSC with GFRP material

The GFRP packaging of the CSSC is achieved using the pultrusion machine (YLJ-15T, Nanjing Haoli Hydraulic Equipment Co., Ltd, Nanjing, China) at Zhixing Technology Nantong Co., Ltd (Nantong, China). The pultrusion machine, depicted in Figure 8(a), comprises the puller, heating die, combiner plate,

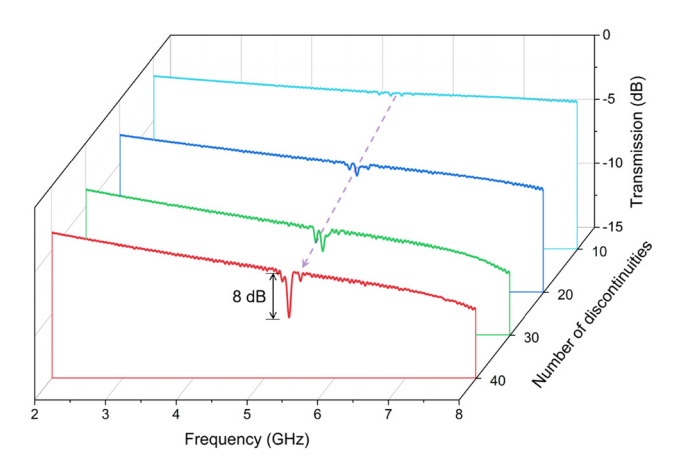


Figure 6: Measured transmission spectrum as the number of discontinuities increased.

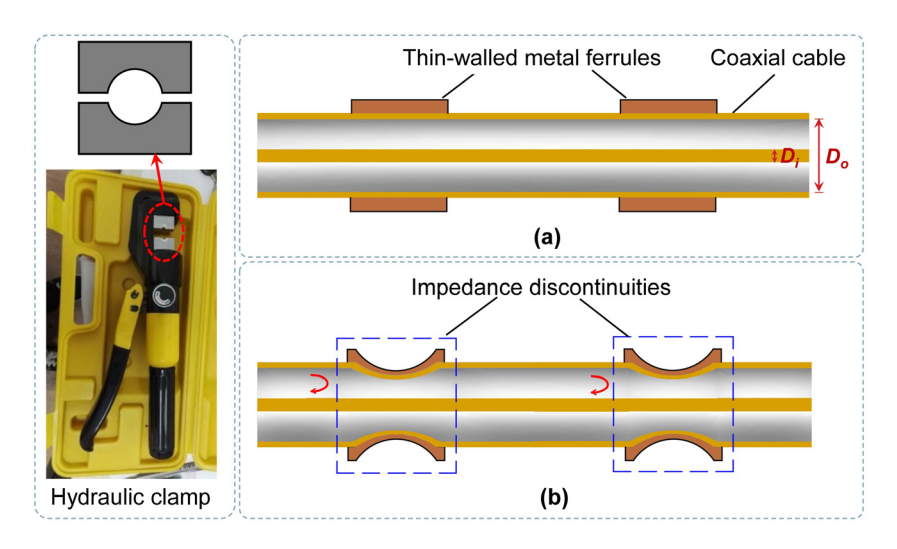


Figure 5: Fabrication procedures of the impedance discontinuities: (a) sleeving thin-walled metal ferrules at specific locations on the cable and (b) crimping of these ferrules.

6 — Tong Jiao et al. DE GRUYTER

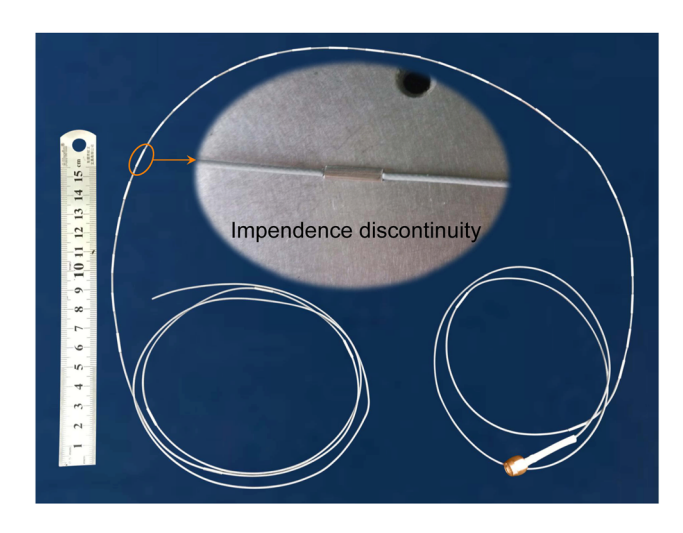


Figure 7: Prototype of the CSSC.

splitting plate, and resin bath. The process schematic is presented in Figure 8(b). The CSSC and 92 threads of unidirectional roving glass fibers (nominal linear density: 9600 Tex; 312T, China Jushi Co., Ltd, Tongxiang, China) are guided through the center and side holes of the splitting and combiner plates, respectively. The fibers pass through a resin bath between the plates, ensuring thorough epoxy resin impregnation. Both CSSC and the impregnated fibers are then pulled into a heating die at a speed of 160 mm·min⁻¹. The die's three zones maintain temperatures of 175, 180, and 150°C, from the

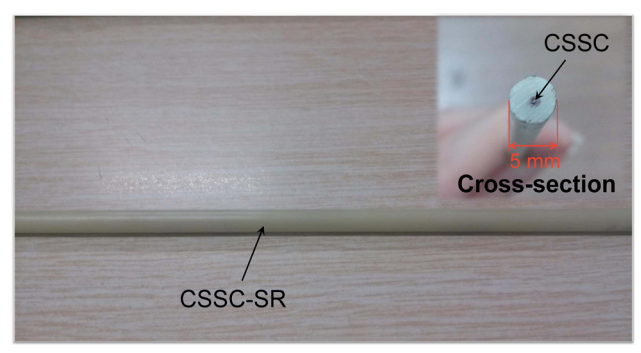


Figure 9: Prototype of the GFRP-SR.

exit to the entrance. This temperature gradient facilitates the resin's cross-linking reaction, enabling polymerization and binding of the CSSC with the fibers. The GFRP-SR is finally fabricated as the cylindrical shape of the given die, as displayed in Figure 9.

2.3.3 Assembly of GFRP-SR with steel wires to create CSSC-ISS

The CSSC-ISS assembly involves substituting the central wire of the standard seven-wire steel strands with the GFRP-SR. The assembly procedures shown in Figure 10 are as follows: (a) evenly wrap the GFRP-SR with a 20–30



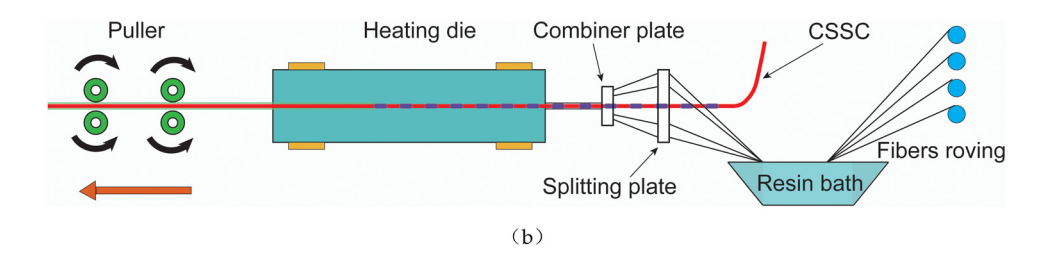


Figure 8: Packaging procedures of CSSC with GFRP material: (a) photo and (b) schematic diagram.



Figure 10: Production procedures of the CSSC-ISS.

mm wide copper foil, ensuring 2–3 layers of foil cover each section of the GFRP-SR; (b) dismantle the seven-wire steel strands corresponding in length to the GFRP-SR, noting the removal sequence for each wire to facilitate subsequent restranding; and (c) re-strand the outer wires onto the GFRP-SR in the opposite order of removal. Before this step, it is necessary to protect the connecting cable at the GFRP-SR's end with copper tubes to prevent the connecting cable from being damaged. The CSSC-ISS can be prepared after the completion of the assembly.

2.4 Experimental investigations

A comprehensive series of laboratory tests were conducted to investigate the properties of CSSC-ISS, as well as its main

components: CSSC and GFRP-SR. An overview of these tests is detailed in Table 1. Notably, all CSSC specimens in this study have a sensing section with a total length of 800 mm, containing 41 impedance discontinuities spaced at 20 mm intervals. The resonant peaks in the reflection and transmission spectrum were gathered using a VNA with a sweep frequency range from 0 to 18 GHz, 16,001 sampling points, and an IF bandwidth of 15 kHz.

2.4.1 Strain sensing test of CSSC

This section presents the experimental evaluation of the signal response characteristics and key sensing performance metrics, such as linearity, accuracy, dynamic range, repeatability, and maximum sensing length, of the

			1 6555 65
Table 1: Mechanical	properties of	the GFKP roa	and GFKP-SK

Sample name	Item	Number of specimens	Objective
CSSC	Static tensile test (0–1,200 με)	1	Investigate the CSSC's signal characteristics, linearity, sensitivity, and resolution
	Static tensile test (0 με-CSSC fails)	3	Investigate the CSSC's range, sensitivity, and accuracy
	Loading-unloading test	1	Investigate the CSSC's repeatability
	Lead cable length test	1	Test the effect of lead cable length on sensing performance
GFRP-SR	Mechanical property test	6	Evaluate whether GFRP-SR has sufficient mechanical strength to replace the central wire in the steel strands
	Static tensile test	3	Investigate the GFRP-SR's signal characteristics, linearity, sensitivity, and accuracy
	Temperature sensing test	1	Investigate the GFRP-SR's temperature sensing capability
CSSC-ISS	Mechanical property test	2	Evaluate whether CSSC-ISS has sufficient mechanical strength
	Static tensile test	3	Investigate the CSSC-ISS's reliability and accuracy in strain and load measurements
	Sustained load tension test	1	Investigate the CSSC-ISS's measurement stability under long- term load

proposed CSSC. Axial tensile tests and loading-unloading tests were executed for this purpose. The test setup incorporated CSSC specimens, a tensioning apparatus, a linear variable displacement transducer (LVDT, SDVH20, Shenzhen Soway Tech. Co., Ltd., Shenzhen, China), a data acquisition system (DH3820N, Donghua Testing Technology Co., Ltd), and a VNA (AV3629D, 14 Research Institute of China Electronics Technology Group Corporation, Bengbu, China) as illustrated in Figure 11. The CSSC specimen was secured on the tensile apparatus with a 1,000 mm gauge length. The apparatus comprised a stationary platform and a movable translation stage for applying axial tensile strain. A pre-strain was applied to the cable prior to testing. To ensure accurate displacement increments, an LVDT with a 100 mm range and 0.0001 mm resolution was equipped on the translation stage. The acquired LVDT readings were captured at a 1 Hz sampling rate, determining the induced strain values.

In the axial tensile test, two distinct tests were conducted on three specimens, namely, CSSC-1, CSSC-2, and CSSC-3. The first test involved 12 displacement increments of 0.1 mm (i.e., 100 $\mu\epsilon$) on CSSC-1 to examine its strain response characteristics, linearity, sensitivity, and resolution. The second test progressively stretched CSSC-1, 2, and 3 until rupture, with 10 mm increments (i.e., 10,000 $\mu\epsilon$) to assess the sensing range, sensitivity coefficient, and accuracy.

For the loading–unloading test on CSSC-4, strain was successively applied and then gradually reduced to zero over three loading cycles, with 1.0 or –1.0 mm increments, correlating to 1,000 or –1,000 $\mu\epsilon$ strains, respectively. Observations were logged every minute to evaluate the CSSC's repeatability. Given the steel strand's general elastic limit strain of under 20,000 $\mu\epsilon$ [44–46], the CSSC's yield strain adequately satisfies testing needs if it encompasses the steel strand's yield strain. Therefore, the tensile threshold was established at 20 mm.

For the lead cable length test, the testing apparatus depicted in Figure 11 is also used. The front end of the CSSC is connected to port 1 of the VNA with 10, 20, 40, and 60 m lead cables, respectively, and the back end of the CSSC is connected to port 2 of the VNA with 1 m lead cables. Initially, the characteristics of the CSSC reflection and transmission spectra were tested for different lead cable lengths. Subsequently, the CSSC was subjected to incremental tensile strain, ranging from 0 to 100,000 $\mu \epsilon$ in 10 mm increments (i.e., 10,000 $\mu \epsilon$). The frequency shift–strain response curve of the CSSC at different lead cable lengths was recorded to evaluate the maximum measurement distance achievable by the CSSC.

2.4.2 Performance test of GFRP-SR

In this section, we conducted a series of lab tests to examine the strain, temperature sensing capabilities, and mechanical properties of the GFRP-SR.

2.4.2.1 Mechanical property test of GFRP-SR

GFRP rod is a structural material with high mechanical strength, which has potential as an alternative to reinforce steel bars in some applications [47–49]. When embedding the CSSC into the GFRP rod to create the GFRP-SR, it is imperative to determine if the GFRP-SR retains sufficient mechanical strength to replace the central wire in steel strands feasibly. For this purpose, we tested three GFRP-SR specimens and three GFRP rods, each 5 mm in diameter. Adhering to the ASTM D7205/D7205M-21 standard [50], the tensile specimen of the composite rod should have a clamping section length of at least 40 times its nominal diameter. Therefore, the length of the sample is 500 mm.

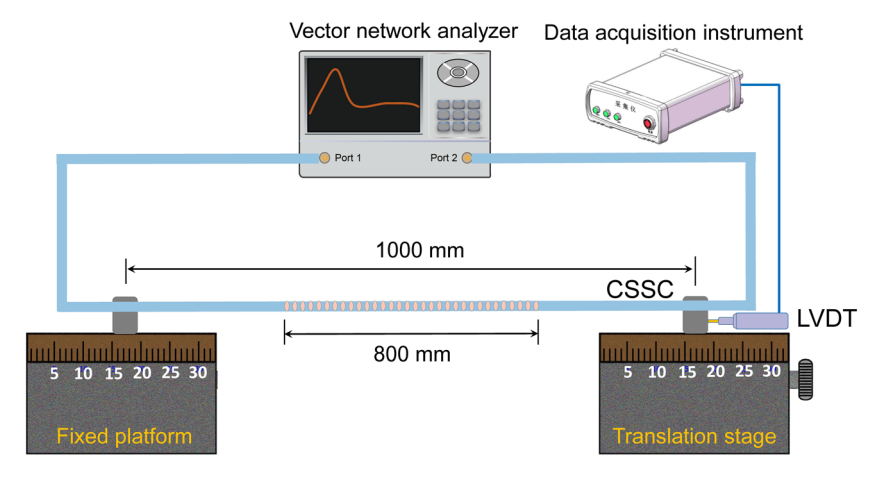


Figure 11: Schematic drawing of the experimental set-up for tensile tests of CSSC.

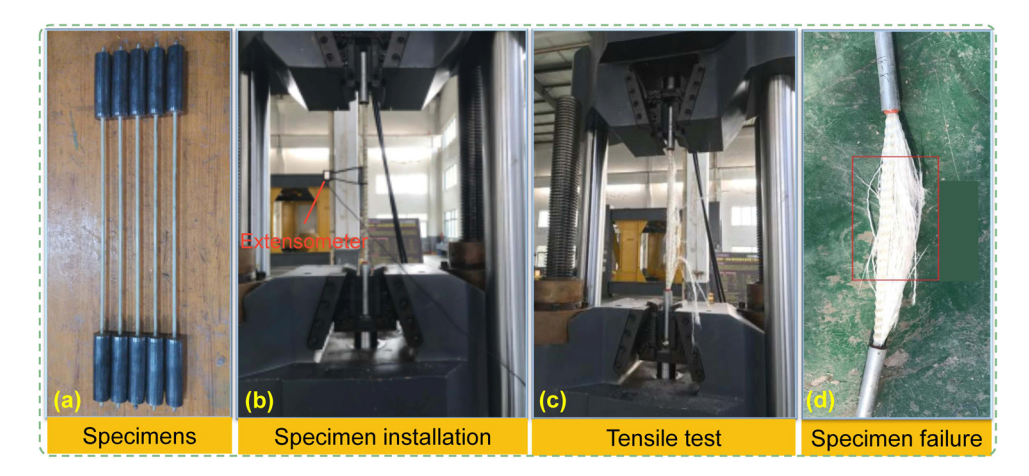


Figure 12: Experimental set-up for mechanical property test of GFRP-SR. (a) Specimens, (b) specimen installation, (c) tensile test, and (d) specimen failure.

To ensure that the tensile machine can firmly clamp the specimens without slippage, two extrusion anchorages with a length of 80 mm were fixed to both ends of the samples [51], as shown in Figure 12(a). Before the tests, the specimens were mounted on the universal test machine (WDW-200E, Jinan Quanli Test Technology Co., Ltd), with a 50 mm gaugelength extensometer attached to measure the tensile strain (Figure 12(b)). The sample was then stretched at 1 mm·min⁻¹ until it was completely damaged (Figure 12(c)). The specimen after tensile failure is shown in Figure 12(d).

2.4.2.2 Strain sensing test of GFRP-SR

DE GRUYTER

A tension test was performed to evaluate the strain-sensing abilities of GFRP-SR. As depicted in Figure 13a, 1,200 mm long GFRP-SR was positioned through a center-hole jack (SL-RRH-3010, Taizhou Soly Machinery Manufacture Co., Ltd,

Taizhou, China), a force transducer with 300 kN range (LTR-1, Shanghai Zhendan Sensor Instrument Factory, Shanghai, China), and a reaction frame. The GFRP-SR was anchored at both ends with an initial distance of 1,000 mm between them. Five electrical resistance strain (ERS) gauges were glued to the GFRP-SR at 200 mm intervals to examine the quantitative strain measurements. A 1 kN step load was applied to the GFRP-SR until its failure. The force transducer data and ERS gauge strain measurements were captured using the DH3820N data acquisition instrument, while the VNA was employed to obtain the GFRP-SR measurements, following the previously mentioned parameter settings.

2.4.2.3 Temperature sensing test of GFRP-SR

The change in strain measurements due to temperature variations should be evaluated to achieve robust stress

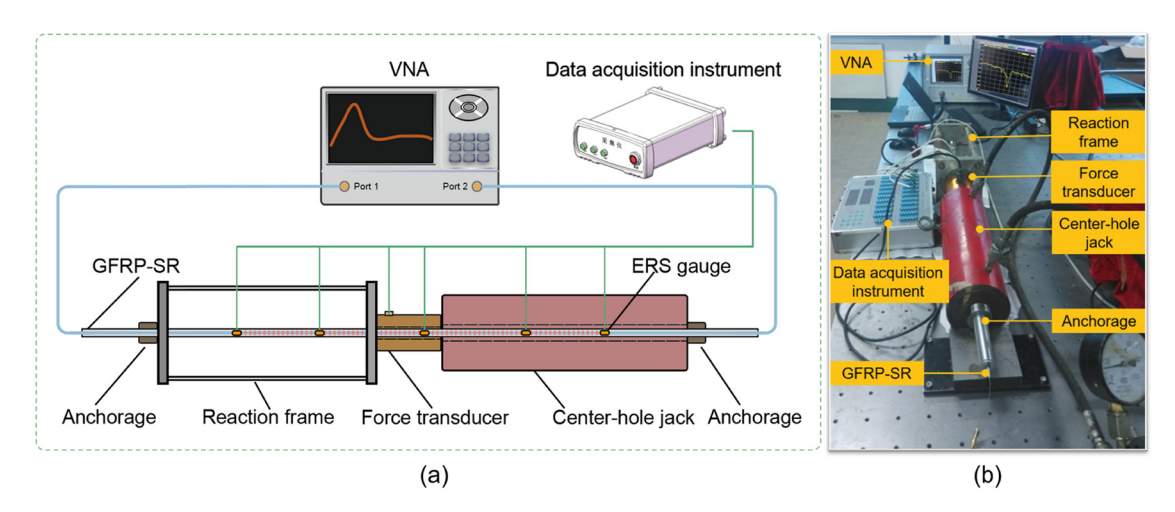


Figure 13: Experimental set-up for strain sensing performance test of GFRP-SR: (a) schematic diagram; and (b) photo.

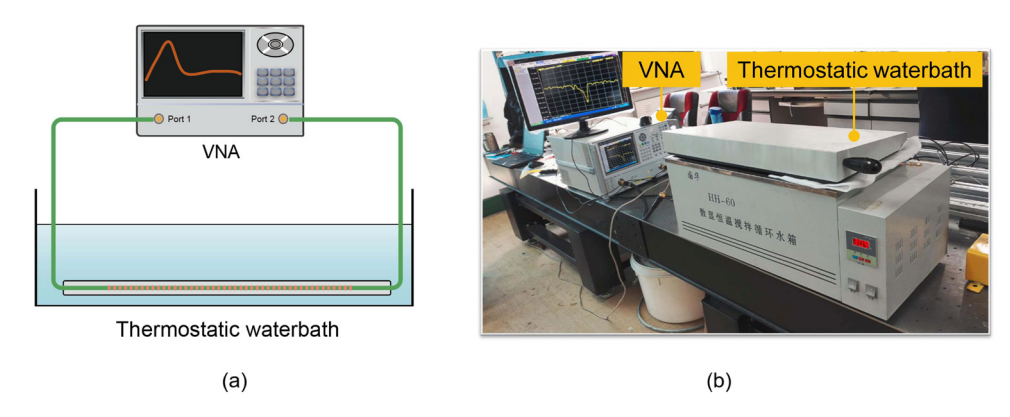


Figure 14: Experimental set-up for temperature sensing performance test of GFRP-SR: (a) schematic diagram; and (b) photo.

monitoring results [52]. GFRP-SR serves as the core sensing element of CSSC-ISS. Therefore, the temperature sensing performance of GFRP-SR was tested to assess the influence of temperature variations on the stress measurement of CSSC-ISS. The temperature sensing capabilities of GFRP-SR were investigated in a controlled environment. A thermostatic water bath (HH-600, Jintan Youlian Instrument Research Institute, Changzhou, China) with a temperature resolution of 0.1°C and an accuracy of \pm 1.0°C was utilized to evaluate a 1,200 mm GFRP-SR. The temperature was progressively raised from 25 to 75°C in increments of 5°C during the examination (Figure 14).

2.4.3 Performance test of CSSC-ISS

2.4.3.1 Mechanical property test of CSSC-ISS

A tensile test was carried out to determine whether the proposed CSSC-ISS has sufficient mechanical strength. The test compared one CSSC-ISS with a standard seven-wire steel strand. Both specimens were anchored on a tensile testing machine with a gauge length of 1 m, as illustrated in Figure 15. The load was incrementally applied at 2 kN·s⁻¹ until specimen failure. The load-displacement curves were derived from the machine's force transducer and displacement gauge.

2.4.3.2 Sensing performance test of CSSC-ISS

Using the apparatus depicted in Figure 16, static tensile tests and sustained load tension tests were performed. The static tests examined the CSSC-ISS's measurement range and accuracy, while the sustained tests assessed its stability under long-term loads. This apparatus closely resembles the one in Figure 13, but it incorporates a high-strength reaction frame and prestressed anchorages designed for steel strands. The spacing between the two anchors was set at 1.2 m. An extensometer was mounted on

the test specimens to provide the actual strain of the CSSC-ISS. Since there is no significant increase in stress once the strand yields, displacement loading was applied to ensure that the data can be effectively recorded throughout the entire tension process. The displacement increment of each step is controlled by deploying an LVDT at the movable end.

Four CSSC-ISS specimens with a total length of 1.4 m were prepared: three for static tensile tests and one for sustained load tension tests. In the static tensile tests, specimens were extended progressively from 0 mm to fracture at 0.9 mm increments. In the sustained load tension tests, the CSSC-ISS was subjected to several constant load levels for 30 min each, with loads set at 30, 90, 150, 210, and 250 kN. Data collection occurred every 5 min. The DH3820N



Figure 15: Experimental set-up for mechanical property test of the CSSC-ISS.

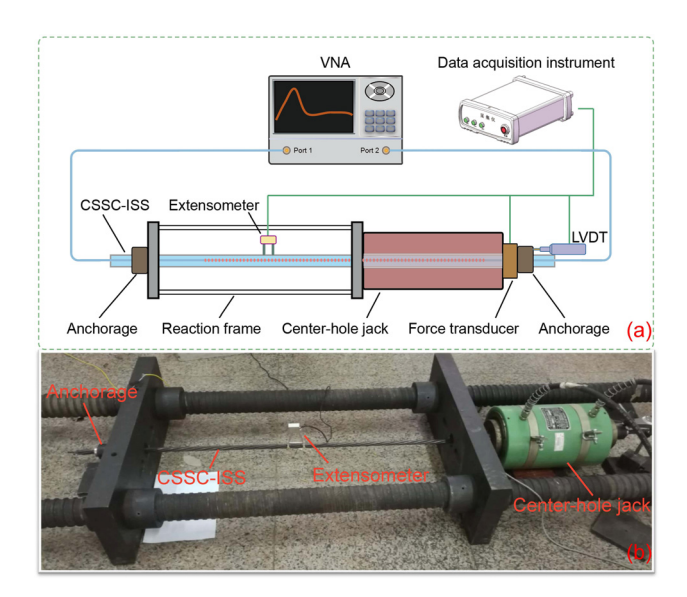


Figure 16: Experimental set-up for strain sensing performance test of CSSC-ISS: (a) schematic diagram; and (b) photo.

data acquisition instrument collected measurements of the extensometer, LVDT, and force transducer, and the measurements of the CSSC-ISS were obtained by the VNA with parameters previously specified.

3 Results and discussion

3.1 Strain sensing results of CSSC

The initial reflection and transmission spectrum of the CSSC specimens were acquired via VNA before testing. Eq. (2) suggests that CSSC specimens with identical parameters should share the same initial resonance frequencies. However, since the specimens were handmade, there will inevitably be production deviation, which will cause slight differences in the initial resonant frequencies. Figure 17 shows the spectrum of the CSSC-1 as an example. Within the frequency sweep bandwidth of 0-18 GHz, three resonant peaks at 5.075, 10.058, and 15.127 GHz can be found in both reflection and transmission spectra. The resonances in the transmission spectrum matched exactly with those in the reflection spectrum. According to Eq. (2), the theoretical resonant frequencies of the CSSC with discontinuities at 20 mm intervals are 5.18, 10.36, and 15.54 GHz. The observed resonant frequencies matched well with those calculated values, with slight differences induced by the deviation between actual and theoretical parameters (i.e., the relative permittivity of dielectric material, spacing of discontinuities). Due to superior SNR in the transmission spectrum's second and third resonant peaks

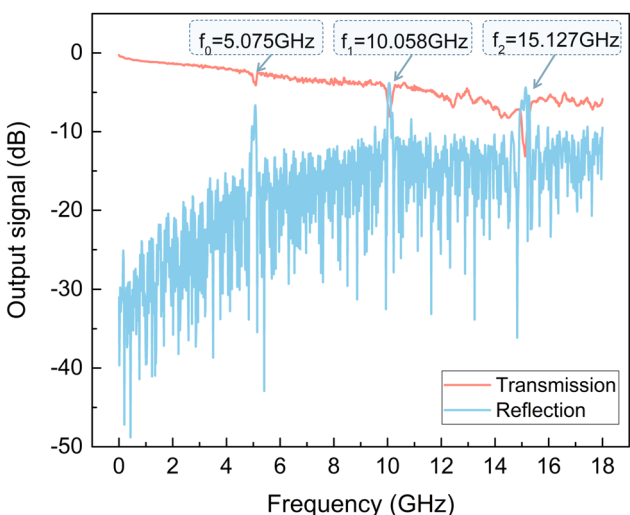


Figure 17: Reflection and transmission spectrum of the fabricated CSSC specimen (CSSC-1).

compared to the reflection spectrum, the second resonant peak, approximately at 10 GHz, is employed for strain calculations.

It should be noted that both transmission spectra and reflection spectra can be utilized for strain calculations. In scenarios where only single-end measurements are feasible, such as monitoring underground structures or long-distance structures, employing reflection spectra for strain calculation is a viable option.

In the axial tensile test ranging from 0 to 1,200 $\mu\epsilon$, Figure 18 demonstrates the resonant frequency's shift with applied tensile strain. The valley monotonically shifted towards lower frequencies as the strain increased at a step of 100 $\mu\epsilon$. The strain–frequency relationship, depicted in Figure 19, exhibits

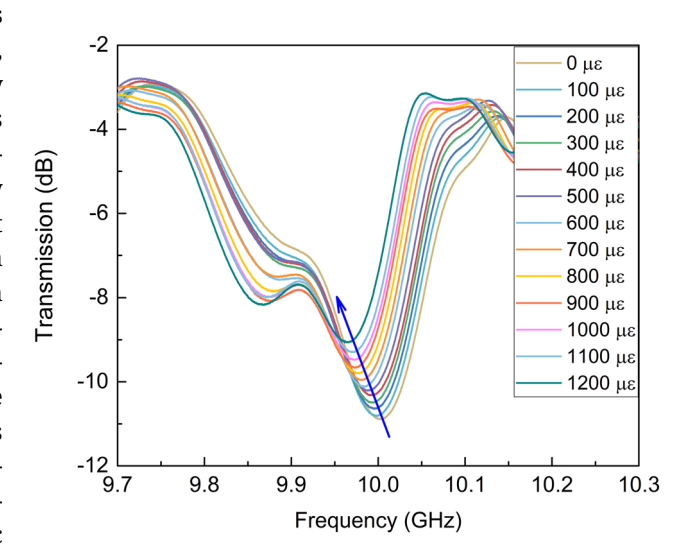


Figure 18: Transmission spectrum shift as strain increased at a step of $100 \ \mu\epsilon$.

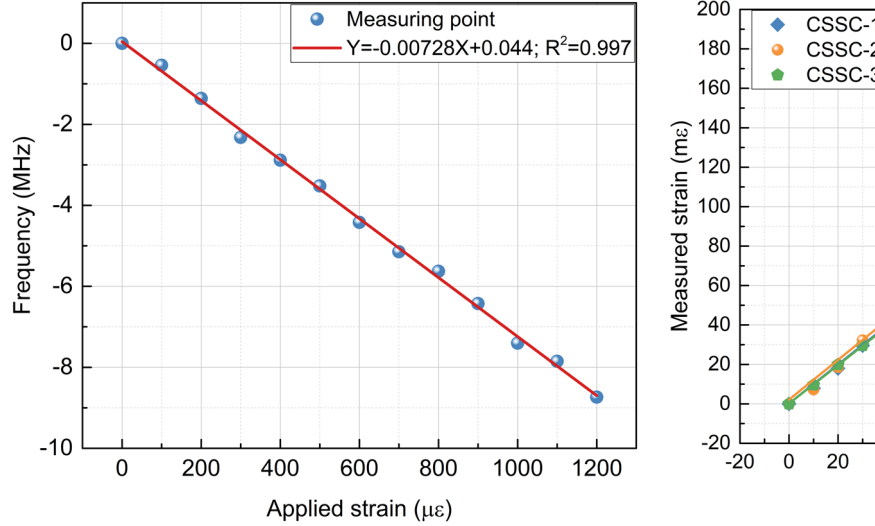


Figure 19: Resonant frequency shift as a function of strain in the 0–1,200 $\mu\epsilon$ range.

remarkable linearity (R^2 = 0.997) with a sensitivity of -7.28 kHz·με⁻¹. These findings suggest that the proposed CSSC can accurately measure tensile strains down to 100 με.

During the axial tensile test, the CSSCs were tested until failure. Figure 20 illustrates that the CSSC-1, 2, and 3 samples failed under tensions exceeding 180,000, 170,000, and 150,000 μ E, respectively. The strain and resonant frequency of the three samples show a good linear relationship, with the correlation coefficients exceeding 0.997. However, the strain sensitivity coefficients of the three CSSCs exhibited a minor dispersion around –7.06k $Hz\cdot\mu\epsilon^{-1}$. This variability primarily arises from fabrication inconsistencies in handmade CSSC specimens. The strains measured by the CSSCs,

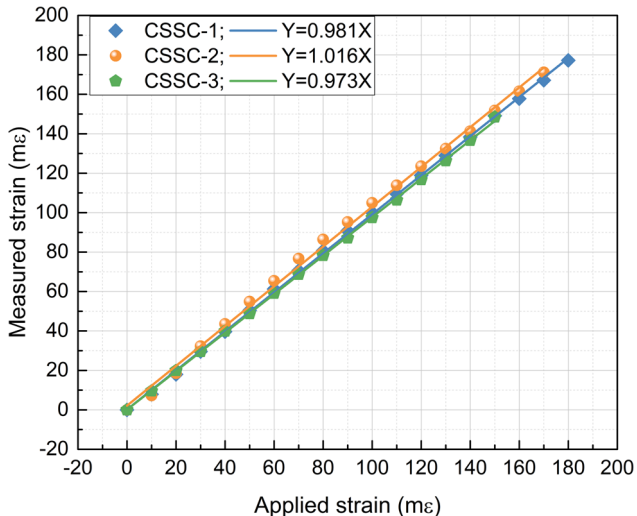


Figure 21: Comparison between strain measurements of CSSC and LVDT.

derived from Eq. (5), were then compared to actual strains from LVDT measurements, as shown in Figure 21. Although the ratios of the measured to actual strains for the three samples approximate 1, they are not strictly equal. This discrepancy can be attributed to the challenges in precisely aligning the theoretical parameters in Eq. (5) with the actual CSSC values. By employing pre-calibration, this deviation can be further reduced to achieve more accurate measurements. The results of the axial tensile test indicate the proposed CSSC features excellent strain-sensing CSSC's exceptional strain-sensing capabilities, emphasizing its potential as a reliable tool for large strain measurement.

In the loading-unloading test, load increments and data recordings were conducted at 1-min intervals, with

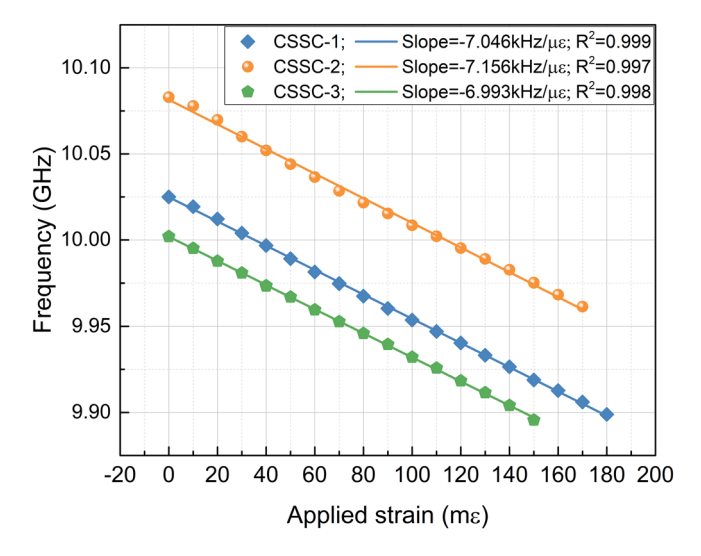


Figure 20: Resonant frequency as a function of strain ranging from 0 με up to the CSSC broke.

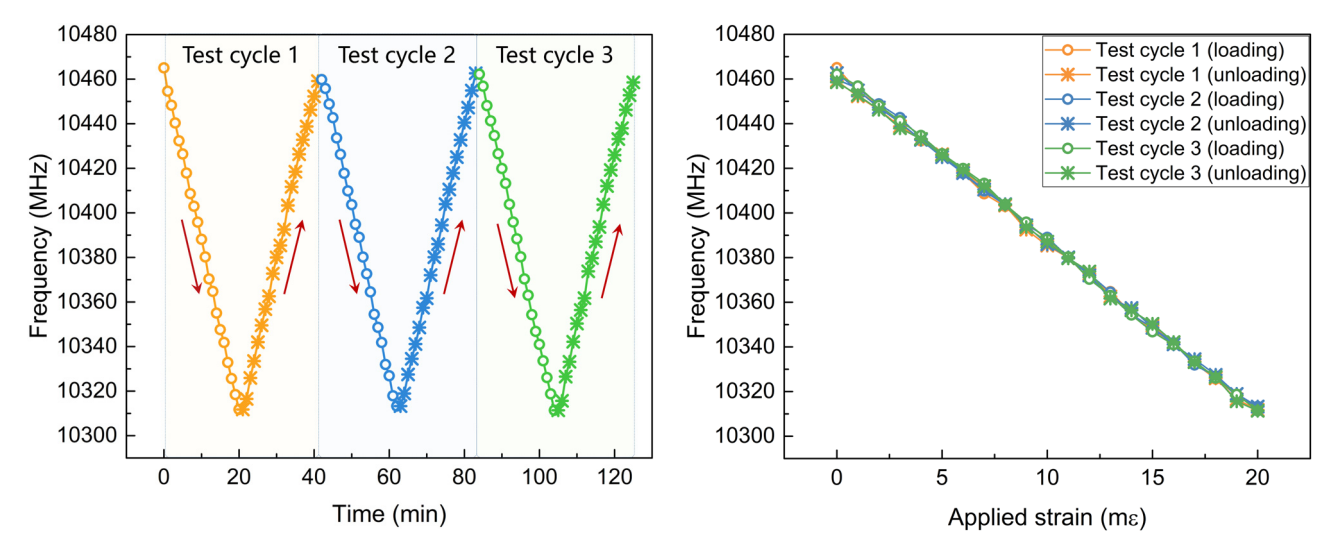


Figure 22: Resonant frequency variation curve over time in the loading-unloading test.

Figure 23: Resonant frequency change of CSSC during three tensile loading cycles.

a total of 126 resonant frequency data recorded, as displayed in Figure 22. The data reveal that as deformation increases, the CSSC's resonant frequency drops and then rises as deformation decreases. After three cycles, the resonant frequency reverts to its initial value. Figure 23 shows the resonant frequency variation curves of the CSSC at different loading–unloading cycles. A high degree of overlapping of data points can be clearly observed in the plot, exhibiting a highly linear response to axial strains up to 20,000 $\mu\epsilon$. No noticeable hysteresis was observed at test completion, highlighting the excellent repeatability of the CSSC in the range of up to 20,000 $\mu\epsilon$.

In the lead cable length test, the reflection and transmission spectra of the CSSC connected to lead cables of different lengths are recorded in Figure 24. It is evident that for lead cable lengths of 10, 20, and 40 m, distinct resonant peaks are observable in both the transmission and reflection spectra. Moreover, the amplitude of these resonant peaks (*i.e.*, the difference between the amplitude of the resonant peak and its adjacent lobes) decreases with the increase in the lead cable length, as indicated in Table 2. To further assess the quality of the sensing signals, the quality factor (Q) is defined herein to quantify the resonance peak quality, expressed as $Q = f/\Delta f$, where f is the

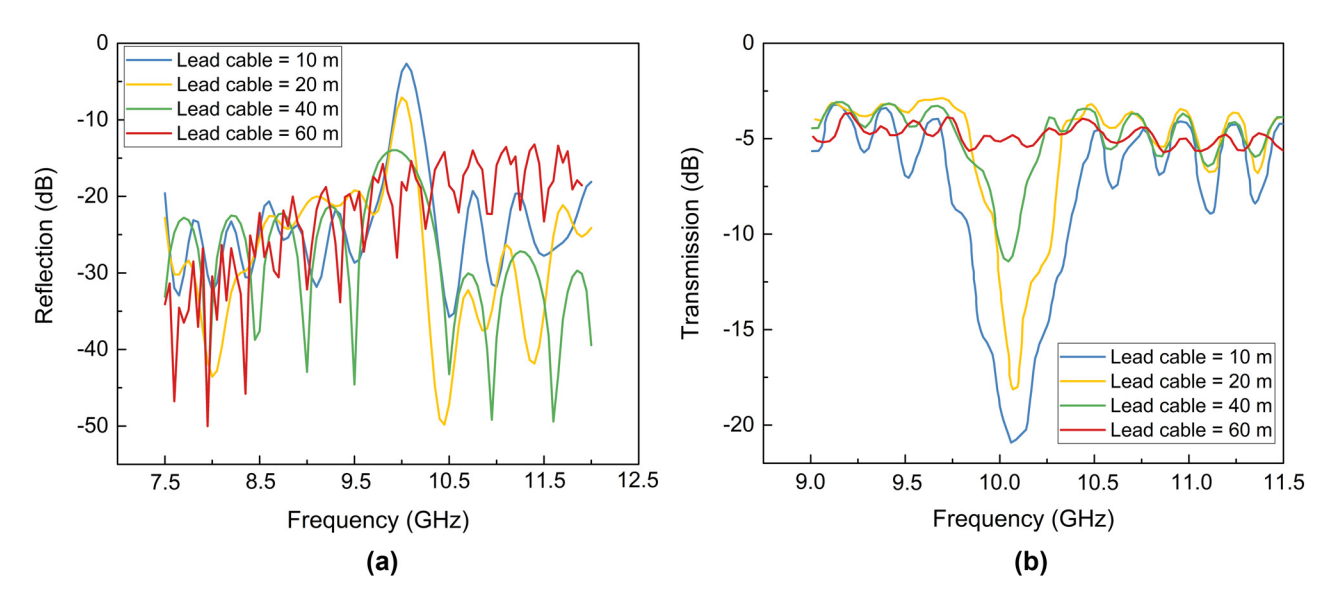


Figure 24: Spectrum of CSSC with lead cables of different lengths: (a) reflection; and (b) transmission.

Table 2: Amplitude and quality factor of CSSC resonant signal with different lead cable length

Items	s Lead cable length (reflection)			Lead cable length (transmission)				
	10 m	20 m	40 m	60 m	10 m	20 m	40 m	60 m
Amplitude	16 dB	12 dB	7 dB	_	13.4 dB	12.21 dB	5.84 dB	_
Q	41.87	55.57	30.93	_	51.54	92.38	42.23	_

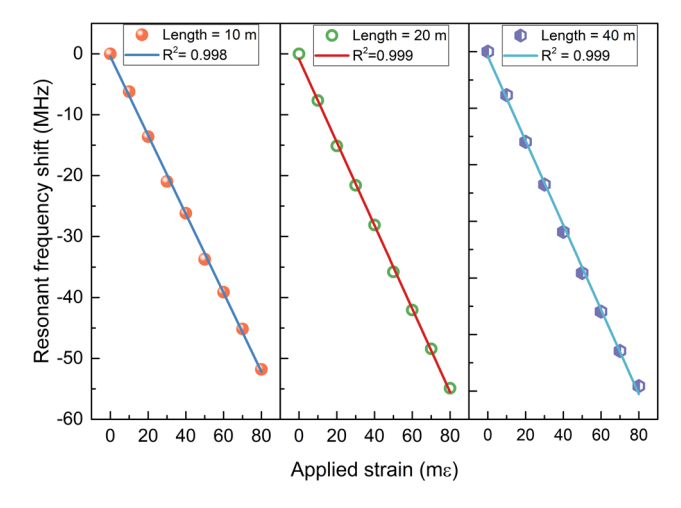


Figure 25: Resonance frequency shift–strain curves of CSSC with different length of lead cables.

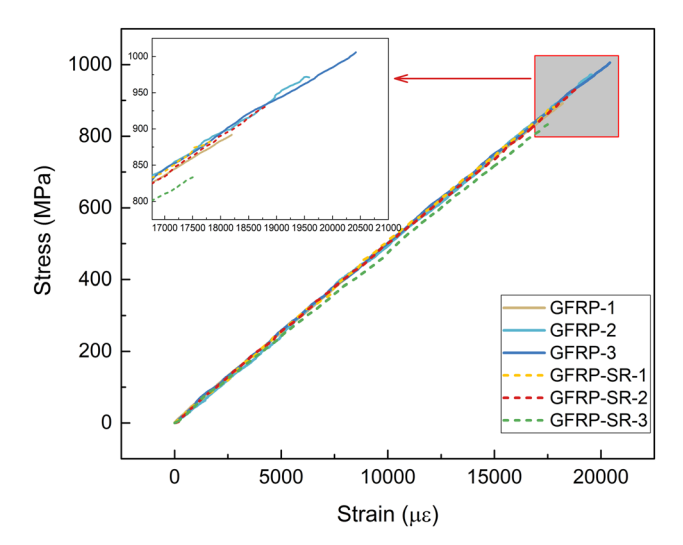


Figure 26: Stress-strain curves of GFRP-SR and GFRP rod.

resonant frequency, and Δf is the 3 dB bandwidth of the resonance peak.

As depicted in Table 2, the quality factor values, exceeding 30 for lead cable lengths not exceeding 40 m, suggest that the resonant peaks exhibit good clarity and SNR, and it is easy to be captured for strain measurement. It can also be seen from Figure 24 that when the length of the lead cable reaches 60 m,

no resonance peak can be observed in both the reflection and transmission spectra. This absence is attributed to significant energy loss in the EM waves transmitted from the VNA through the 60 m lead cable to the CSSC. It indicates that CSSC, as a localized sensor, needs to make the length of the lead cable less than 60 m when used.

To investigate whether the length of the lead cable affects the sensing performance of the CSSC, tensile tests were conducted on CSSC connected with 10, 20, and 40 m lead cables, respectively, and the results measured from the transmission spectrum are shown in Figure 25. It is observed that, irrespective of the length of the lead cable, the resonant peak frequency shift of CSSC has a good linear relationship with the strain. Additionally, there is no discernible difference in the linearity of these relationships, as evidenced by the linear fitting correlation coefficients exceeding 0.998 for all cases. It implies that when the length of the lead cable does not exceed 40 m, variations in lead cable length do not significantly impact the sensing performance of the CSSC.

3.2 Results of performance tests of GFRP-SR

3.2.1 Mechanical properties of GFRP-SR

The stress-strain curves obtained from the mechanical tests reveal the characteristics of both GFRP-SR and GFRP rods. Figure 26 demonstrates that both materials exhibit ideal elastic behaviors. While their elastic moduli are comparable, the GFRP-SR has a slightly lower strain limit than the GFRP rod. Table 3 provides detailed mechanical properties of each sample, including tensile strength, elastic modulus, and strain limit. It shows that the average strain limit for GFRP-SR is approximately 7% less than the GFRP rod. However, the variation in strain limits for both materials makes this difference statistically insignificant. Regarding tensile strength, GFRP-SR's average is 882 MPa, which is 92.3% of the GFRP rod's 956 MPa. This reduction can be attributed to the lower tensile strength of CSSC in GFRP-SR. These results show that the mechanical properties of GFRP-SR remain robust, reinforcing its potential as a suitable substitute for the central wire in steel strands.

Table 3: Mechanical properties of the GFRP rod and GFRP-SR

Specimens	Tensile strength (MPa)		Elasticity modulus (GPa)		Strain limit (%)	
	Value	Average	Value	Average	Value	Average
GFRP -1	892	956	48.8	49.2	18,199	19,400
GFRP-2	971		49.7		19,584	
GFRP-3	1,006		49.1		20,417	
GFRP-SR-1	882	882	49.6	48.5	17,816	18,048
GFRP-SR-2	931		48.3		18,801	
GFRP-SR-3	834		47.7		17,527	

3.2.2 Strain sensing properties of GFRP-SR

Prior to testing, we evaluated the impact of the GFRP packaging behavior on the CSSC sensing signals. Figure 27 illustrates the transmission and reflection spectra variations of CSSC before and after being packaged with GFRP. The sensing spectra of the GFRP-SR (*i.e.*, CSSC packaged by GFRP) align well with the initial spectra prior to packaging, retaining its spectral shape without distortion. While the GFRP-SR spectrum displays consistent resonance peaks that match with that of the CSSC, there's a minor decline in the resonance peak, attributed to the pre-tension exerted on the CSSC before packaging. However, this does not impede its sensing capabilities. These results show that GFRP-SR has good sensing signal quality and verify the feasibility of the pultrusion process of GFRP for CSSC described above.

During the tensile test, GFRP-SR-1, 2, and 3 ruptured at tensile loads of 16, 16, and 15 kN, respectively. Figure 28 demonstrates that the resonant frequency shifts of these specimens are linearly correlated with the applied load. Their sensitivity coefficients are 9.92, 10.31, and 9.11 MHz·kN⁻¹,

gest that, with proper calibration, the proposed GFRP-SR can serve both as a structural component and a force sensor.

Figure 29 provides a quantitative comparison between the strain measurements obtained from GFRP-SR and ERS gauges. The average strain readings from five ERS gauges are used as the reference value in this plot. The strain measurements of the GFRP-SR coincide with those of the ERS gauge, with the slopes of the former being higher than the latter. In regions of minimal deformation, their relative discrepancies exceed 10%. However, as deformation increases,

respectively. The variance in these sensitivity coefficients is because it is hard to achieve the exact parameters of the

different hand-made CSSC in GFRP-SR, resulting in the devia-

tion of their initial resonant frequencies. These findings sug-

are used as the reference value in this plot. The strain measurements of the GFRP-SR coincide with those of the ERS gauge, with the slopes of the former being higher than the latter. In regions of minimal deformation, their relative discrepancies exceed 10%. However, as deformation increases, these discrepancies diminish, reaching lows of under 5%. Calibration inaccuracies in GFRP-SR are the primary contributors to these errors. If a more accurate calibration is employed, the differences between the GFRP-SR and ERS results can be reduced. The findings indicate that GFRP-SR can measure strain reliably and accurately. A noteworthy advantage of

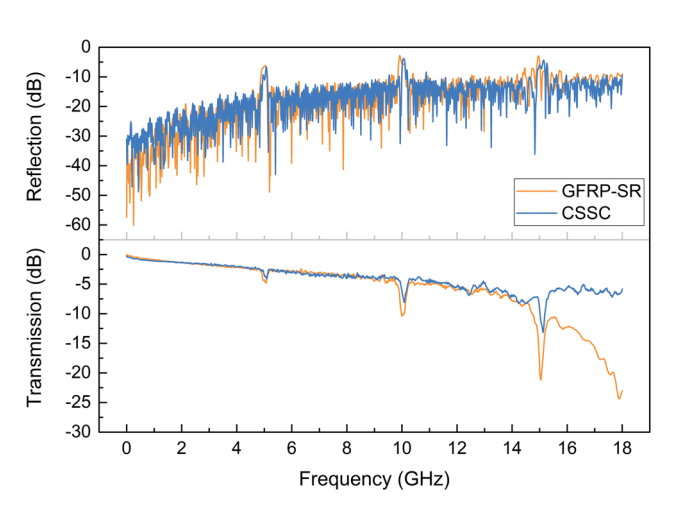


Figure 27: Spectrum of the CSSC before and after being packaged with GFRP.

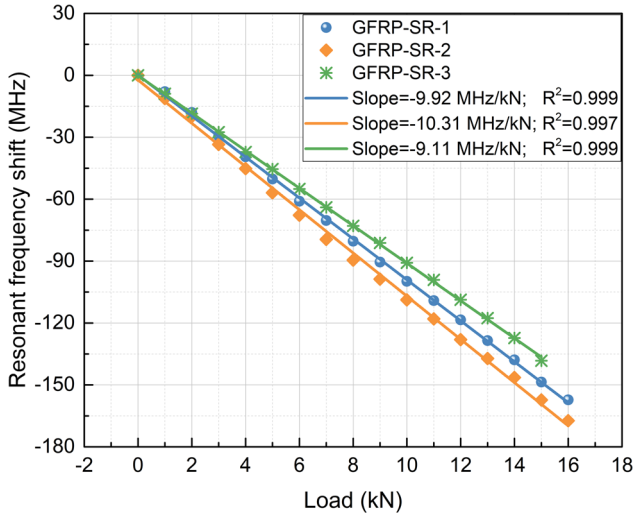


Figure 28: Resonant frequency shifts of three GFRP-SR specimens with increasing load.

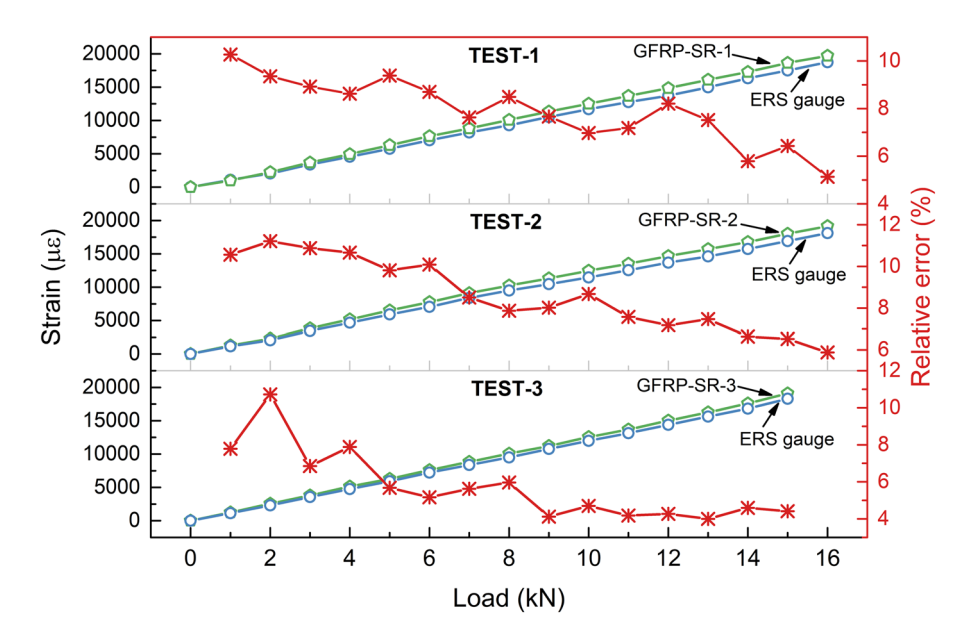


Figure 29: Comparison between strain measurements of GFRP-SR and ERS gauge.

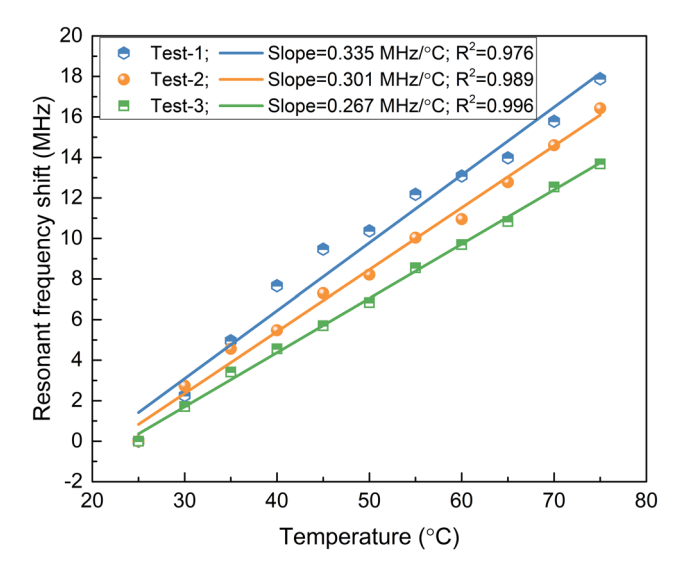
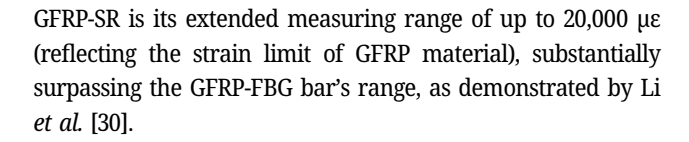


Figure 30: Resonant frequency shifts of three GFRP-SR specimens with the increase in the temperature.



3.2.3 Temperature sensing properties of GFRP-SR

In the temperature-sensing test presented in Figure 30, the resonant frequency shifts of GFRP-SR demonstrate a linear relationship with temperature, with a sensitivity of about

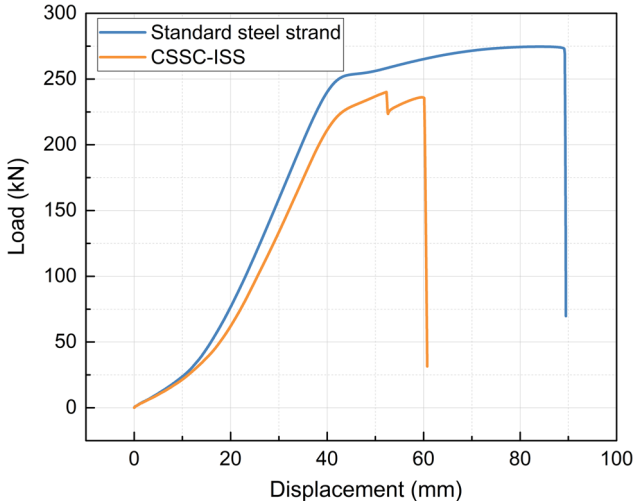


Figure 31: Load–displacement curves of CSSC-ISS and standard steel strand.

0.3 MHz·°C⁻¹. This suggests that GFRP-SR has the potential to function as a temperature sensor. According to the force sensitivity of GFRP-SR, which is about 10 MHz·kN⁻¹, a temperature fluctuation of 1°C corresponds to a force variation of around 30 N. This indicates that temperature compensation is not necessary for applications where measurement accuracy is not strictly required. If precise stress measurements are required, a non-loaded GFRP-SR can be parallelly attached to the CSSC-ISS. The temperature compensation for CSSC-ISS can then be achieved by subtracting the frequency shift of the GFRP-SR from the frequency shift measured by CSSC-ISS.

Table 4: Mechanical properties of the standard steel strand and the proposed CSSC-ISS

Specimens	Maximum force (kN)	Yield force (kN)	Tensile strength (MPa)	Elasticity modulus (GPa)
Standard steel strand	272	253	1,922	186
CSSC-ISS	239	226	1,689	165

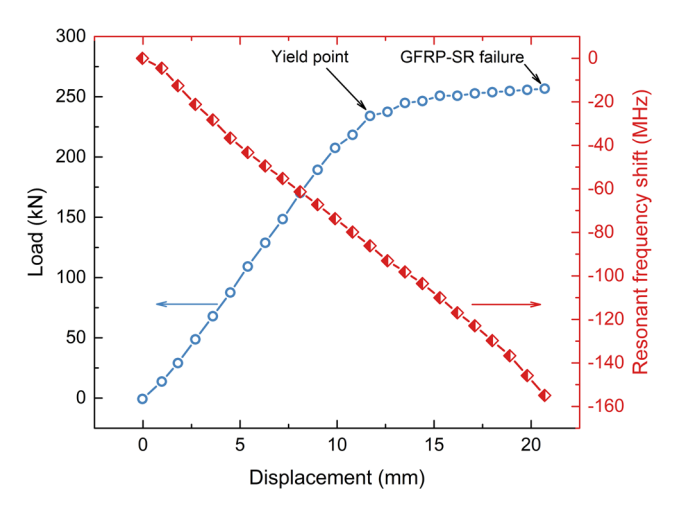


Figure 32: The variations in load and resonant frequency shift of CSSC-ISS in the whole loading process.

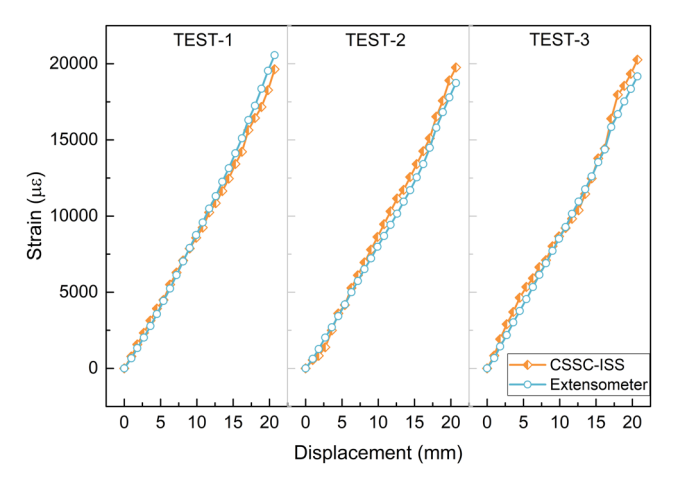


Figure 33: Comparison of strain measurements between CSSC-ISS and extensometer.

3.3 Results of performance tests of CSSC-ISS

3.3.1 Mechanical properties of CSSC-ISS

Figure 31 illustrates the load-displacement curves for both CSSC-ISS and the standard seven-wire steel strands, exhibiting similar ductile failure characteristics. The CSSC-ISS curve differs notably with a short region from yield to break and a pronounced dip. This dip arises because,

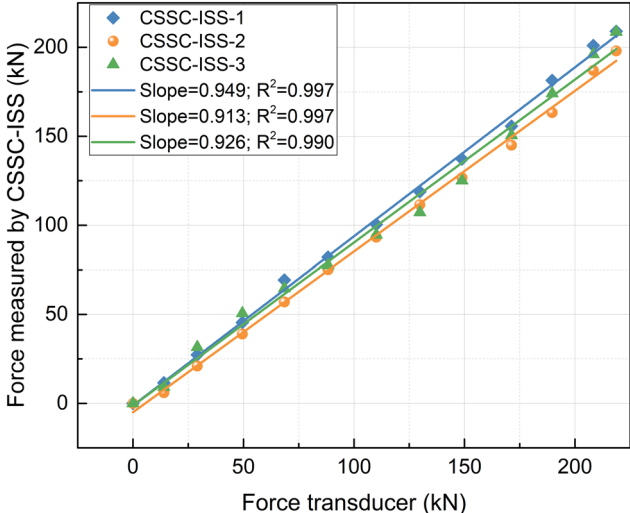


Figure 34: Tension results determined by the CSSC-ISS.

upon reaching the peak load, the difference in elastic moduli causes the six outer wires to separate readily from the central GFRP-SR. Table 4 presents the mechanical properties of these specimens. Specifically, the tensile strength and elastic modulus of the CSSC-ISS are 87.9 and 88.7% of those of the standard steel strand, respectively. These results suggest that while the CSSC-ISS's mechanical properties are marginally different from the standard steel strand, it could serve as a partial replacement, offering inherent self-sensing capabilities for structures.

3.3.2 Sensing properties of CSSC-ISS

During the tensile tests, the CSSC-ISS is deemed to fail when the tensile displacement reaches 20.7 mm, at which point the GFRP-SR breaks. The load variation curve and the resonant frequency shift curve are plotted together in Figure 32, where the load data are the force transducer measurements. The figure reveals that the resonant frequency shift diminishes linearly as the strand stretches. Notably, even beyond the yield point, the frequency shift retains a good linear correlation with the displacement. The results verify that the CSSC embedded in GFRP-SR has a good response to external tension, which means that the GFRP-SR can codeform with the outer wire of the strand.

18 — Tong Jiao et al. DE GRUYTER

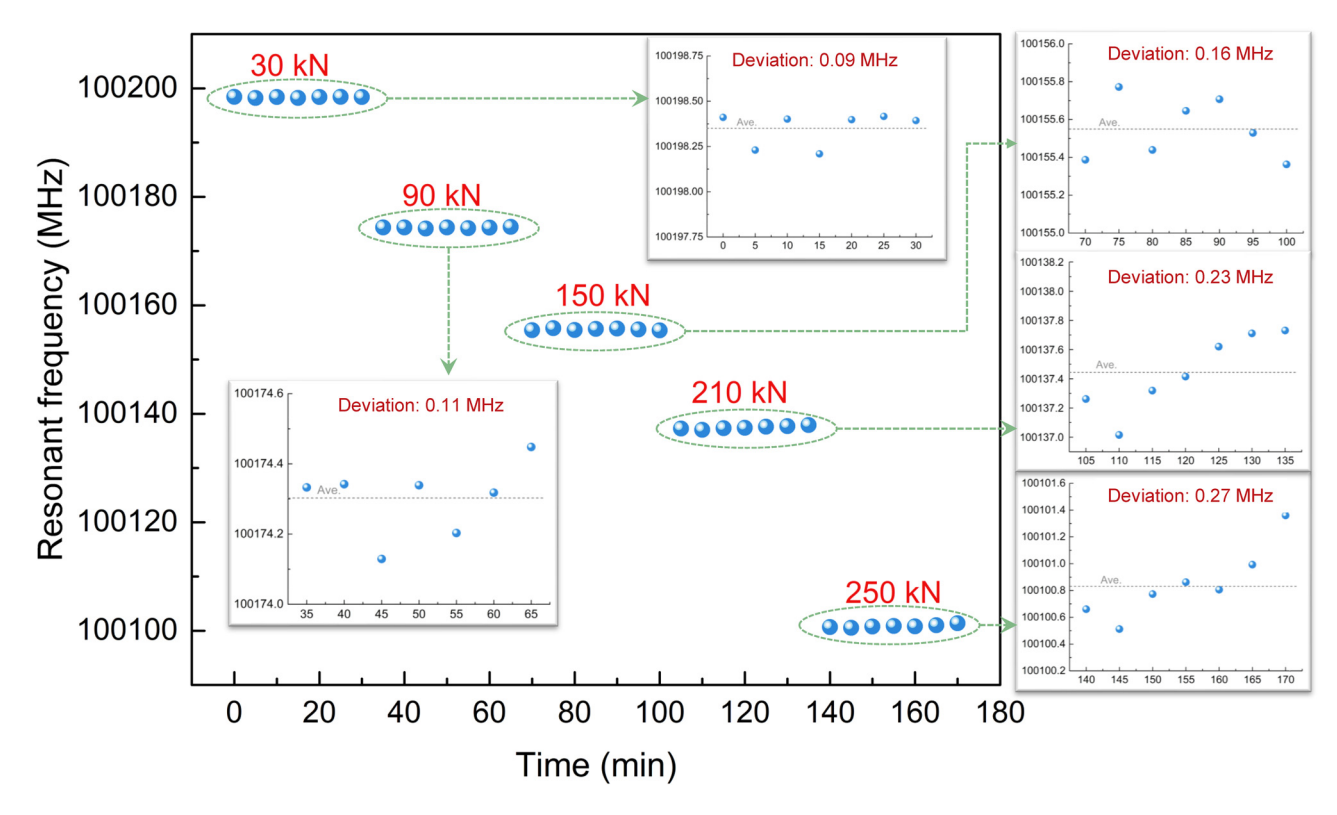


Figure 35: Resonant frequencies of the CSSC-ISS under the sustained loads of different amplitudes.

To assess the accuracy of the strain and load measurements from the CSSC-ISS quantitatively, Figures 33 and 34 present the comparison of strain and load values measured by CSSC-ISS with their actual values, respectively. Figure 33 displays a linear relationship between the three CSSC-ISS strain readings and the tensile displacements. Furthermore, it agrees well with the strain derived from extensometer readings, demonstrating the reliability and accuracy of the CSSC-ISS's self-sensing capability. The tension of the CSSC-ISS can be determined by utilizing Eq. (1) based on its measured strain. Figure 34 plots the tension results from the three CSSC-ISS specimens against applied loads, with the horizontal axis denoting force transducer readings. The three fitting curves have a high linear fit, with slopes of 0.949, 0.913, and 0.926, respectively. A slope closer to 1 indicates a closer alignment of measured to actual values. The findings reveal a maximum relative error of under 8.7%. These errors are mainly because the strain value used in load calculation is calculated by substituting the calibration coefficient of GFRP-SR into Eq. (5). If the CSSC-ISS is calibrated directly, the measurement error is expected to be greatly reduced.

Figure 35 presents the results from the sustained load tension test. During each 30-min load stage, the resonant frequency of the CSSC within GFRP-SR remains remarkably consistent. Even at a high load of 250 kN, the standard

deviation is a mere 0.27 MHz. Since the sensitivity factor approximates 10 MHz·kN⁻¹, this deviation only introduces a negligible fluctuation in the measured value of about 0.027 kN. This result proves that the proposed CSSC-ISS has a stable measurement capability under long-term load in practical engineering.

4 Conclusion

Aiming at the challenge where current stress measurement techniques for steel strands cannot cover the entire process from initial tension to failure, this study proposed a large stress-tolerated steel strand (i.e., CSSC-ISS), which has both functions of force-bearing and self-sensing. The CSSC-ISS was achieved by embedding an innovative CSSC, capable of large strain measurements, into the steel strand as its sensing unit. Extensive laboratory tests were conducted on the core components (CSSC and GFRP-SR) and the CSSC-ISS itself. The key findings include:

a) A small-diameter CSSC with a high-quality signal can be fabricated by crimping more than 40 equidistant thinwalled metal ferrules (acting as impedance discontinuities) onto the SF047 coaxial cable. This CSSC exhibits distinct resonant peaks or dips in both its transmission and reflection spectrums. These frequencies decline linearly with the increase in strain. The test results show that the CSSC can measure strains up to 150,000 $\mu\epsilon$ with a resolution of at least 100 $\mu\epsilon$. Furthermore, it has good repeatability in the range of 20,000 $\mu\epsilon$, which can cover the elastic deformation range of the steel strand.

b) The CSSC is a localized sensor accommodating lead cable lengths up to 40 m. In scenarios where only two ends of a steel strand bear tension with a uniform stress distribution (e.g., suspension cables in bridges, suspension cables in large-span spatial structures), and where stress is uniformly distributed along the length, CSSC can be strategically placed with lead cables at the midsection of the steel strand to facilitate stress measurement. For steel strands experiencing complex stress distributions with significant variations (e.g., slope anchor rods), multiple CSSCs can be installed at different locations along the steel strand. Subsequently, a costeffective multi-channel demodulator for CSSC can be employed, connecting various CSSCs to distinct channels, thereby enabling quasi-distributed measurements. This CSSC demodulator can be easily assembled using conventional electronic components such as voltage-controlled oscillators, central processing units, detectors, phase shifters, circulators, and amplifiers, ensuring low-cost demodulation.

c) The GFRP-SR was innovatively designed by encapsulating the CSSC within GFRP material. After this encapsulation, the CSSC's sensing signal quality remains consistent, affirming the feasibility of the proposed packaging technique. The GFRP-SR exhibits consistent linear responses to both strain and temperature. However, its resonant frequency's sensitivity to strain significantly surpasses that to temperature, making temperature compensation unnecessary for rough strain measurements. Notably, the strain measurement range of GFRP-SR is the ultimate strain of GFRP material, about 20,000 µE, which is much higher than that of GFRP-FBG bar with only 6,000 µE as documented in prior research. The innovative GFRP-SR can serve not only as the central sensing component of the CSSC-ISS but also as a standalone sensor for strain or temperature monitoring tasks.

d) In comparison to standard steel strands, the CSSC-ISS exhibits slightly subdued mechanical properties. Specifically, its tensile strength and elastic modulus reach 87.9 and 88.7% of the standard steel strand's values, respectively. However, while retaining a substantial bearing capacity, the CSSC-ISS offers accurate, reliable, and stable sensing of its own strain and load. Its measurement range can cover the ultimate load of the steel strand. It is pivotal to recognize that although the load-bearing capacity of CSSC-ISS is not as good as that of standard steel strands, its application potential remains undiminished. This is because multiple steel strands are

integrated into an integral load-bearing unit in many real-world applications, like pre-stressed anchor cables. By substituting only one or a few strands within these multi-strand configurations with the CSSC-ISS, the impact of CSSC-ISS on the overall load capacity is minimal. In conclusion, the CSSC-ISS stands out as a novel solution, enabling continuous stress-state monitoring throughout its lifecycle without affecting its load-bearing ability.

Acknowledgments: Special thanks are due to Prof. Jinping Ou and Prof. Zhi Zhou of Dalian University of Technology. The findings and opinions expressed in this article are only those of the authors and do not necessarily reflect the views of the sponsors.

Funding information: This work was financially supported by the National Natural Science Foundation of China (Grant Nos 42107210, 42107096, and 42107208), Major Program of the National Natural Science Foundation of China (Grant No. 41941019), China Postdoctoral Science Foundation (Grant No. 2023M730377), Youth program of Natural Science Foundation of Sichuan Province (Grant No. 2022NSFSC112), Open Research Fund of State Key Laboratory of Geohazard Prevention and Geoenvironment Protection (Grant No. SKLGP2022K022), and also by Sichuan Province Science and Technology Support Program (Grant No. 2021YFSY0036).

Author contributions: For the work reported in this article, Tong Jiao proposed the idea of CSSC integrated steel strand; Tong Jiao, Qiang Xu, Minggao Tang, and Xing Zhu conceived and designed the study; Chuhong Pu, Chuankun Liu, and Jiang Li designed and performed the experiments, and analyzed the data; Tong Jiao and Chuhong Pu wrote and edited the manuscript. All authors have accepted responsibility for the entire content of this manuscript and approved its submission.

Conflict of interest: The authors state no conflict of interest.

References

- [1] Shi, H., J. Zhao, F. Chen, J. Lin, and J. Xie. Mechanical behaviour of precast prestressed reinforced concrete beam–column joints in elevated station platforms subjected to vertical cyclic loading. *Reviews on Advanced Materials Science*, Vol. 60, No. 1, 2021, pp. 818–838.
- [2] Ahlborn, T. M., C. K. Shield, and C. W. French. Full-scale testing of prestressed concrete bridge girders. *Expedition Technology*, Vol. 21, No. 1, 1997, pp. 33–35.
- [3] Zhang, Y., Z. Fang, R. Jiang, Y. Xiang, H. Long, and J. Lu. Static performance of a long-span concrete cable-stayed bridge

- subjected to multiple-cable loss during construction. *Journal of Bridge Engineering*, Vol. 25, 2020, id. 04020002.
- [4] Liu, X., B. Wu, and C. He. A novel integrated sensor for stress measurement in steel strand based on elastomagnetic and magnetostrictive effect. P. Tse, Mathew, J., Wong, K., et al. (Eds.), Engineering Asset Management Systems, Professional Practices and Certification, Springer International Publishing, Cham, 2015, pp. 65–73.
- [5] Chaki, S. and G. Bourse. Guided ultrasonic waves for nondestructive monitoring of the stress levels in prestressed steel strands. *Ultrasonics*, Vol. 49, No. 2, 2009, pp. 162–171.
- [6] Scalea, F. L., P. Rizzo, and F. Seible. Stress measurement and defect detection in steel strands by guided stress waves. *Journal of Materials in Civil Engineering*, Vol. 15, No. 3, 2003, pp. 219–227.
- [7] Li, X., B. Zhang, C. Yuan, T. Chong, D. Chen, Z. Chen, et al. An electromagnetic oscillation method for stress measurement of steel strands. *Measurement*, Vol. 125, 2018, pp. 330–335.
- [8] Zhang, S., J. Zhou, K. Tan, H. Zhang, J. Qian, H. Liu, et al. A prestress testing method for the steel strands inside in-service structures based on the electrical resistance. *Measurement*, Vol. 184, 2021, id. 109930.
- [9] Zhang, X., L. Zhang, L. Liu, and L. Huo. Prestress monitoring of a steel strand in an anchorage connection using piezoceramic transducers and time reversal method. *Sensors*, Vol. 18, No. 11, 2018, id. 4018.
- [10] Zhang, S., H. Zhang, J. Zhou, H. Liu, H. Ma, and L. Liao. Alternating prestress monitoring of steel strands based on the magnetoelastic inductance method. *Measurement*, Vol. 194, 2022, id. 111024.
- [11] Ni, Y., Q. Zhang, and R. Xin. Magnetic flux detection and identification of bridge cable metal area loss damage. *Measurement*, Vol. 167, 2021, id. 108443.
- [12] Liu, S., C. Cheng, R. Zhao, J. Zhou, and K. Tong. A stress measurement method for steel strands based on spatially self-magnetic flux leakage field. *Buildings*, Vol. 13, No. 9, 2023, id. 2312.
- [13] Le, T. C., T. T.V. Phan, T. H. Nguyen, D. D. Ho, and T. C. Huynh. A low-cost prestress monitoring method for post-tensioned RC beam using piezoelectric-based smart strand. *Buildings*, Vol. 11, No. 10, 2021, id. 431.
- [14] Nguyen, T. T., N. D. Hoang, T. H. Nguyen, and T. C. Huynh. Analytical impedance model for piezoelectric-based smart strand and its feasibility for prestress force prediction. *Structural Control Health Monitoring*, Vol. 29, No. 11, 2022, id. 3061.
- [15] Wang, H., X. Gong, X. Wang, S. Feng, T. Yang, and Y. Guo. Discrete curvature-based shape configuration of composite pipes for local buckling detection based on fiber Bragg grating sensors. *Measurement*, Vol. 188, 2022, id. 110603.
- [16] Wang, H., J. Dai, and X. Wang. Improved temperature compensation of fiber Bragg grating-based sensors applied to structures under different loading conditions. *Optical Fiber Technology*, Vol. 63, 2021, id. 102506.
- [17] Zhu, W., Q. Shen, and H. Qin. Monitoring of prestress and bond stress of self-sensing FBG steel strand. *Measurement*, Vol. 177, 2021, id. 109246.
- [18] Williams, C., M. Khatri, P. Okumus and R. Holt. Post-tensioning force measurement using optical fiber sensor-embedded strand for prestressed concrete structures. A. Ilki, Çavunt, D., and Çavunt, Y. S., (Eds.), *Building for the Future: Durable, Sustainable, Resilient*, Springer Nature Switzerland, Cham, 2023, pp. 622–633.
- [19] Nakaue, S., K. Oshima, M. Oikawa, M. Nishino, Y. Matsubara, and M. Yamada. "SmART Strand" prestressing steel strand with optical fiber for tension monitoring. *Sumitomo Denki*, Vol. 92, 2021, pp. 62–67.

- [20] Imai, M., K. Okubo, N. Sogabe, H. Tobe, M. Oikawa, S. Nakaue et al. Stress distribution monitoring of ground anchor using optical fiber-embedded strand. *Proceeding SPIE 10970, Sensors and Smart Structures Technologies for Civil, Mechanical, and Aerospace Systems*, Vol. 10970, 2019, id. 109701 J.
- [21] Abdel-Jaber, H. and B. Glisic. Monitoring of long-term prestress losses in prestressed concrete structures using fiber optic sensors. Structural Health Monitoring, Vol. 18, No. 1, 2019, pp. 254–269.
- [22] Zhou, Z., J. He, G. Chen, and J. Ou. A smart steel strand for the evaluation of prestress loss distribution in post-tensioned concrete structures. *Journal of Intelligent Material Systems and Structures*, Vol. 20, No. 16, 2009, pp. 1901–1912.
- [23] Lan, C., Z. Zhou, and J. Ou. A novel GFRP-FBG smart steel strand and its properties research. *Applied Mechanics and Materials*, Vol. 105–107, 2012, pp. 1087–1091.
- [24] Lan, C., Z. Zhou, and J. Ou. Full-scale prestress loss monitoring of damaged RC structures using distributed optical fiber sensing technology. *Sensors*, Vol. 12, No. 5, 2012, pp. 5380–5394.
- [25] Lan, C., Z. Zhou, and J. Ou. Monitoring of structural prestress loss in RC beams by inner distributed Brillouin and fiber Bragg grating sensors on a single optical fiber. *Structural Control Health Monitoring*, Vol. 21, No. 3, 2014, pp. 317–330.
- [26] Kim, J. M., H. W. Kim, Y. H. Park, I. H. Yang, and Y. S. Kim. FBG sensors encapsulated into 7-wire steel strand for tension monitoring of a prestressing tendon. *Advances in Structural Engineering*, Vol. 15, 2012, pp. 907–918.
- [27] Kim, S. T., H. Yoon, Y. H. Park, S. S. Jin, S. Shin, and S. M. Yoon. Smart sensing of PSC girders using a PC strand with a built-in optical fiber sensor. *Applied Sciences*, Vol. 11, No. 1, 2021, id. 359.
- [28] Kim, J. M., H. W. Kim, S. Y. Choi, and S. Y. Park. Measurement of prestressing force in pretensioned UHPC deck using a fiber optic FBG sensor embedded in a 7-wire strand. *Journal of Sensors*, Vol. 2016, 2016, id. e8634080.
- [29] Kim, J. M., Y. S. Kim, H. W. Kim, D. N. Seo and C. B. Yun. Development of smart tendon instrumented with optical FBG sensors. *Proceedings of the Computational Structural Engineering Institute Conference*, 2007, pp. 33–38.
- [30] Li, D., Z. Zhou, and J. Ou. Development and sensing properties study of FRP–FBG smart stay cable for bridge health monitoring applications. *Measurement*, Vol. 44, No. 4, 2011, pp. 722–729.
- [31] Kim, S. T., Y. H. Park, S. Y. Park, K. Cho, and J. R. Cho. A sensor-type PC strand with an embedded FBG sensor for monitoring prestress forces. *Sensors*, Vol. 15, No. 1, 2015, pp. 1060–1070.
- [32] Kim, J. M., C. M. Kim, S. Y. Choi, and B. Y. Lee. Enhanced strain measurement range of an FBG sensor embedded in seven-wire steel strands. *Sensors*, Vol. 17, No. 7, 2017, id. 1654.
- [33] Habel, J., T. Boilard, J. S. Frenière, F. Trépanier, and M. Bernier. Femtosecond FBG written through the coating for sensing applications. *Sensors*, Vol. 17, No. 11, 2017, id. 2519.
- [34] Barrias, A., J. Casas, and S. Villalba. A review of distributed optical fiber sensors for civil engineering applications. *Sensors*, Vol. 16, No. 5, 2016, id. 748.
- [35] Mizuno, Y., A. Theodosiou, K. Kalli, S. Liehr, H. Lee, and K. Nakamura. Distributed polymer optical fiber sensors: a review and outlook. *Photonics Research*, Vol. 9, No. 9, 2021, id. 1719.
- [36] Wei, T., S. Wu, J. Huang, H. Xiao, and J. Fan. Coaxial cable Bragg grating. Applied Physics Letters, Vol. 99, No. 11, 2011, id. 113517.
- [37] Huang, J., T. Wei, X. Lan, J. Fan and H. Xiao. Coaxial cable Bragg grating sensors for large strain measurement with high accuracy.

- Proceeding SPIE 8345, Sensors and Smart Structures Technologies for Civil, Mechanical, and Aerospace Systems, Vol. 8345, 2012, id. 83452Z.
- [38] Huang, J., T. Wei, S. Wu, X. Lan, J. Fan, and H. Xiao. Coaxial cable Bragg grating sensors for structural health monitoring.

 International Journal of pavement Research and Technology, Vol. 5, No. 5, 2012, pp. 338–342.
- [39] Stevan Jr, S. L., J. J.A. Mendes Júnior, F. C. Janzen, and M. L. Oliveira. Long period Bragg grating in coaxial transmission lines. J Microwaves. Optoelectronic and Electromagnetic Applications, Vol. 14, No. 1, 2015, pp. 28–39.
- [40] Huang, J., T. Wang, L. Hua, J. Fan, H. Xiao, and M. Luo. A coaxial cable Fabry-Perot interferometer for sensing applications. *Sensors*, Vol. 13, No. 11, 2013, pp. 15252–15260.
- [41] Jiao, T., Z. Zhou, and H. Xiao. Investigation into coaxial cable Fabry–Perot interferometers for strain measurement and crack detection in RC structures. *Measurement*, Vol. 147, 2019, id. 106873.
- [42] Huang, J., X. Lan, W. Zhu, B. Cheng, J. Fan, Z. Zhou, et al. Interferogram reconstruction of cascaded coaxial cable Fabry-Perot interferometers for distributed sensing application. *IEEE Sensors Journal*, Vol. 16, No. 11, 2016, pp. 4495–4500.
- [43] Huang, J. Coaxial cable Bragg grating. Master dissertation. Missouri University of Science and Technology, Rolla, Missouri, USA, 2012.
- [44] Shakya, A. and V. Kodur. Effect of temperature on the mechanical properties of low relaxation seven-wire prestressing strand. *Construction and Building Materials*, Vol. 124, 2016, pp. 74–84.
- [45] Kim, J. K. and J. M. Yang. Effect of design variables on deflected tensile performance of high-strength 7-wire steel strand for stay cable. Construction and Building Materials, Vol. 188, 2018, pp. 40–48.

- [46] Jeon, C. H., J. B. Lee, S. Lon, and C. S. Shim. Equivalent material model of corroded prestressing steel strand. *Journal of Materials Research and Technology*, Vol. 8, No. 2, 2019, pp. 2450–2460.
- [47] Cai, Y., S. Xiao, Y. Chen, Z. Huang, J. Lin, Y. Guo, et al. Tensile behavior and durability prediction of GFRP-steel composite bars under chloride environments. *Journal of Materials Research and Technology*, Vol. 23, 2023, pp. 5746–5759.
- [48] Al-Furjan, M. S. H., L. Shan, X. Shen, M. S. Zarei, M. H. Hajmohammad, and R. Kolahchi. A review on fabrication techniques and tensile properties of glass, carbon, and Kevlar fiber reinforced polymer composites. *Journal of Materials Research and Technology*, Vol. 19, 2022, pp. 2930–2959.
- [49] Ren, Y., H. Wang, Z. Guan, and K. Yang. Evaluation of the properties and applications of FRP bars and anchors: A review. Reviews on Advanced Materials Science, Vol. 62, No. 1, 2023, pp. 1–34.
- [50] ASTM D7205. Standard test method for tensile properties of fiber reinforced polymer matrix composite bars, ASTM International, West Conshohocken, PA, 2017.
- [51] Lian, S., O. Jinping, and Z. Zhi. Development of a new anchorage system for carbon fiber-reinforced polymer rods using extrusion process. *Advances in Structural Engineering*, Vol. 25, No. 5, 2022, pp. 1002–1014.
- [52] Huynh, T. C. and J. T. Kim. FOS-based prestress force monitoring and temperature effect estimation in unbonded tendons of PSC girders. *Journal of Aerospace Engineering*, Vol. 30, No. 2, 2017, id. B4016005.